ELSEVIER

International Journal of Mass Spectrometry 200 (2000) 357–386

International Journal of Mass Spectrometry

Vacuum ultraviolet photoionization and photoelectron studies in the new millennium: recent developments and applications

C.Y. Ng*

Ames Laboratory, United States Department of Energy, and Department of Chemistry, Iowa State University, Ames, Iowa 50011, USA

Received 7 July 2000; accepted 23 August 2000

Abstract

Vacuum ultraviolet (VUV) photoionization mass spectrometry and photoelectron spectroscopy have played a central role in providing energetic and spectroscopic information for neutrals and cations. The most important data obtainable in a VUV photoionization and photoelectron experiment are ionization energies and 0 K ion dissociation thresholds or appearance energy (AE), from which 0 K bond dissociation energies for neutrals and cations can be deduced. The recent developments in VUV lasers and third-generation synchrotron sources, together with the introduction of the pulsed-field ionization (PFI), photoelectron (PFI-PE), and PFI-photoion (PFI-PI) methods, have revolutionized the field of photoelectron and ion spectroscopy by significantly improving the energy resolution to the range of 0.025–1.0 meV (full width at half maximum, FWHM). These resolutions, which make possible the measurement of photoelectron spectra for many simple molecules at the rotational-resolved level, are ≈100-fold better than those observed in traditional photoelectron studies, making the PFI-PE technique a true spectroscopic method. The recent introduction of the synchrotron-based PFI-PEPICO scheme has shown that AE values for a range of molecules can be determined with an unprecedented precision limited only by the PFI-PE measurement. The synchrotron-based PFI-PEPICO and PFI-PI schemes show great promises for future studies of state- or energy-selected ion-dissociation dynamics and energy-selected ion-molecule reaction dynamics. Further improvement in energy resolution for PFI-PE and PFI-PI measurements has been demonstrated using the two-color photo-induced Rydberg ionization (PIRI) spectroscopic scheme, which involves the photo-induced ionization of intermediate long-lived high-n ($n \geq 100$) Rydberg states. The incorporation of this method by VUV photoexcitation to prepare intermediate high-n ($n \geq 100$) Rydberg states is also expected to greatly increase the energy range of PFI studies. The availability of this array of laser- and synchrotron-based PFI methods, including PFI-PE, PFI-PEPICO, PFI-PI, PFI-ion-pair, and PIRI schemes, ensures an exciting and bright future for VUV photoionization and photoelectron studies in the new millennium. (Int J Mass Spectrom 200 (2000) 357–386) © 2000 Elsevier Science B.V.

Keywords: Photoionization; Photoelectron; Pulsed field ionization; Vacuum ultraviolet; Synchrotron radiation; Photoelectron-photoion coincidence

1. Introduction

Modern photoionization mass spectrometry and photoelectron spectroscopy using a tunable vacuum ultraviolet (VUV) photon source can be traced back to the laboratory of Inghram at the University of Chicago.[1,2] Vigorous developments of this field in the past 50 yr have had a major impact in ion chemistry and photoionization dynamics.[3–10] A primary concern in mass spectrometric studies is the ability to

* E-mail: cyng@ameslab.gov

PII S1387-3806(00)00348-1

determine the chemical structure (or atomic connectivity) of the neutral sample molecule based on the observed ion masses and ion intensity distribution. This requires basic knowledge about molecular ionization and fragmentation induced by excitation of photons and electrons, which are commonly used as the ionization sources to convert neutral sample molecules into charge particles before mass analyses. Accurate energetic data,[4,5] such as ionization energies (IEs) and 0 K ion dissociation energies or appearance energies (AEs), determined for a broad range of molecular species are fundamental for understanding the ion intensity pattern observed in the mass spectrum of a neutral molecular sample. For this reason, photoionization efficiency (PIE) measurements, which can provide relative photoionization cross sections and reliable IE and AE values for neutral species, are of great interest to many researchers belonging to the mass spectrometry community.

From the chemistry point of view, the main motivation for IE and AE measurements are stemmed from the fact that IE and AE values are directly related to 0 K bond dissociation energies (D_0) of neutrals and cations. As D_0 values for molecular species are used to predict the feasibility of chemical reactions, accurate IE and AE measurements are of fundamental importance to chemistry. On the basis of energy conservation, the IE for a molecule ABC (IE[ABC]) and the AE for producing the fragment ion AB^+ (AE[AB^+]) from ABC are related to the D_0 for the AB^+–C bond (D_0[AB^+–C]) by the equation

$$D_0(AB^+–C) = AE(AB^+) - IE(ABC). \quad (1)$$

If the IE for the neutral AB radical (IE[AB]) is known, the D_0 for the neutral AB-C bond (D_0[AB–C)] can also be calculated according to a similar equation,

$$D_0(AB–C) = AE(AB^+) - IE(AB). \quad (2)$$

If energies for the excited ABC^+, AB^+, and AB states relative to their respective ground states are known from spectroscopic measurements, binding energies of excited ABC^+ and ABC can also be determined. Eqs. (1) and (2) show that the precision for $D_0(AB^+–C)$ and $D_0(AB–C)$ thus obtained depends on the uncertainties of AE(AB^+), IE(ABC), and IE(AB). In traditional photoionization and photoelectron measurements using laboratory discharge lamps and second-generation synchrotron radiation sources, the uncertainties for IE and AE values obtained for polyatomic species usually fall in the range of ≈30–150 meV.[4,5]

The major advances in photoionization and photoelectron measurements in the past decade can be attributed to the development of VUV lasers [8,11–14] and third-generation synchrotron radiation [15,16] sources. The tunable range for VUV lasers with usable photon intensities has been extended to ≈19 eV. The recently established high-resolution monochromatized VUV synchrotron facility at the Advanced Light Source (ALS) covers the energy range of 8–30 eV [17–22]. The availability of these VUV sources has induced the development of novel experimental schemes for photonion and photoelectron studies [17–35].

Because of page limitations and of the broad scope of this subject, it is not possible to give a detailed account here of all aspects of recent advances in the field of photoionization and photoelectron studies. Fortunately, major reviews and progress reports on important areas of this field have been made recently [8–10]. Taking this into consideration, I have limited the scope of this article to photoionization and photoelectron studies using tunable VUV sources. In "Experimental Advances" below, I have outlined recent experimental developments and briefly discussed the associated principles. Possible future developments and applications are also speculated on. Since the present article is not intended to be a thorough review and the topics chosen here purely reflect the interest of the author, omission of other important topics and references cannot be avoided. Because of the involvement of this author, a more detailed discussion is given for recent synchrotron-based high-resolution photoionization and photoelectron studies [15–22].

2. Experimental advances

2.1. Photoionization efficiency measurements

The photoionization efficiency (PIE) of a photoion is measured by the ratio of the photoion intensity

(I[ion]) to the photon intensity (I[photon]) at a given photon energy. The measurement of the PIE spectra (or the relative photoionization cross sections) of photoions observed in the photoionization of a gaseous sample is the primary concern in photoionization mass spectrometric studies. Photoionization efficiency measurements obtained at a sufficiently high resolution provide the most fundamental and useful data for probing autoionization mechanisms for Rydberg states converging to excited ionic states. Because of the relatively simple experimental arrangement, the majority of IE and AE values available in the literature were obtained by PIE measurements [4,5]. We note that AE values that are determined on the basis of PIE measurements can suffer a large uncertainty because of the hot band and kinetic shift effects,[4] particularly for ion dissociation processes involving polyatomic species. For previous reviews on PIE measurements, readers are referred to Refs. [6,16,36–38].

When an autoionization Rydberg series is resolved in a PIE experiment covering a sufficiently large number of Rydberg states, its analysis can lead to a highly precise converging limit or IE value. For example, the IE values for the HCO radical (IE=8.15022±0.00006 eV)[39] and benzene (IE=9.243842±0.000006 eV)[40] determined by the Rydberg series extrapolation method are among the most accurate IE values known. The resolutions of PIE measurements are limited not only by the VUV optical bandwidths but also by the electric field used or existing at the photoionization region. A finite electric field is usually needed for the extraction of photoions produced at the photoionization. Such an electric field is known to induced Stark mixings of Rydberg levels associated with different orbital angular momenta, resulting in the broadening of peak widths of autoionizing Rydberg states [41,42]. Thus, in order to obtain the highest possible resolution in PIE measurements, it is necessary to minimize the residual electric field at the photoionization region.

2.1.1. PIE sampling of nascent photodissociation products

A recent interesting application of VUV photoionization mass spectrometry involves the determination of chemical structures for nascent photofragments formed in laser photodissociation reactions [36,37,43–47]. One of the important objectives for a photochemical study is to identify the primary photoproduct structures and branching ratios for dissociation channels at a known photodissociation wavelength. For polyatomic product species with unknown spectroscopic properties, laser spectroscopic detection schemes may not be useful for product structure identifications. Since photoionization mass spectrometry is a mass and energy sensitive technique, the VUV PIE measurement of a primary photoproduct near its ionization threshold can, in principle, be used effectively to identify its chemical structure. Although polyatomic molecules and radicals may exist in many isomeric forms, their IEs are often sufficiently different to allow an unambiguous identification of the isomers involved. However, primary photofragments often contain internal excitations. As a result, the experimental IE observed for a photoproduct is expected to shift to a lower energy, depending on the exothermicity of the specific photochemical process. To overcome this problem, it is possible to cool the primary photoproducts in a supersonic expansion before PIE measurements. This can be accomplished by inducing the photochemical process in the high-pressure region of a free jet, that is, close to the nozzle tip. It has been well demonstrated that further expansion of the photoproducts together with the bath molecules or atoms can be an effective means of relaxing the internal photoproduct excitations. If the sample gas consists of a small fraction of the precursor molecules seeded in an unreactive carrier gas, such as a rare gas, secondary reactions of the photoproducts can be minimized. In principle, the distortion of primary photoproduct branching ratios caused by secondary processes can be examined by varying the precursor gas to rare gas ratio.

This photodisssociation-photoionization (PD/PI) approach, which involves photoionization mass spectrometric sampling of laser photodissociation products in a pulsed supersonic molecular beam, has been successfully applied to identify the isomeric structures of the 193-nm photofragments from thiophene [47]. On the basis of the comparison of IE values deter-

mined in PIE measurements for $C_2H_2^+$, $C_2H_2S^+$, and $C_4H_4^+$ ions, Hsu [47] concluded that the primary neutral photofragments formed are vinylacetylene (H_2C=CH–C≡CH), acetylene (C_2H_2), and thioketene (H_2C=C=S), indicating that the major dissociation channels are CH_2=CH–C≡CH+S(^3P) and CH≡CH+CH_2=C=S. In the 193-nm photodissociation of CH_3SH, CH_3CH_2SCH, and CH_3SSCH_3, the primary photofragments are found to have the CH_3S, CH_3CH_2S, and CH_3SS structures, respectively [43–46]. The success of these experiments shows that this PD/PI method holds great promise as a general method for structural determination of nascent products formed in photochemical reactions.

2.2. Threshold photoelectron spectroscopy

As a result of the strongly predissociative nature of polyatomic molecules in excited Rydberg states, autoionizing Rydberg features for polyatomic species are often found to be very weak in their PIE spectra. In such cases, the PIE spectrum may only provide information about the first IE. The photoelectron spectrum often contains more information on the energetics and spectroscopy for the excited cation than that revealed in its PIE spectrum. Hence, the development of high-resolution photoelectron spectroscopic techniques has been a primary pursuit in the field of photoionization and photoelectron studies.

Threshold photoelectrons (TPEs) are near-zero kinetic energy electrons (ZEKEs), which are formed slightly above the true IE [47–49]. It is well established that the intensities for TPE bands observed using a tunable VUV source are governed not only by the Franck-Condon factors (FCFs) for direct ionization but also by nearby resonance autoionization mechanisms [9]. The later mechanisms make possible the observation of photoelectron bands with near-zero FCFs. Consequently, photoelectron bands for highly excited vibronic states close to their dissociation limits can be readily observed. As a spectroscopic tool, the TPE method is preferred over the HeI and HeII studies [50,51], where the observable ionization transitions are mostly limited by the FCFs.

The first TPE experiment to search for ionization thresholds using a tunable VUV source was made by Inghram and coworkers in 1967[2]. This was followed 2 yr later by Schlag and coworkers [48] and Sphor et al.[49], who introduced the steradiancy discrimination scheme for TPE detection. Since TPEs can be collected with high efficiency into a narrow solid angle using a small electrostatic field, the TPE method has been the preferred technique for photoelectron studies when a tunable VUV light source is used. The steradiancy discrimination of energetic electrons has been traditionally achieved by using a tubelike structure for defining the solid angle for electron detection. Assuming that background energetic electrons are ejected over a large solid angle, they would be greatly discriminated. However, finite energetic electrons ejected along the steradiancy analyzer would still be detected. This gives rise to a hot tail in the TPE transmission function, which has limited the achievable resolution for TPE measurements. When a pulsed VUV source with a sufficiently long time separation (>100 ns) between adjacent light pulses is used, the hot-tail problem in TPE detection can be alleviated by the electron time-of-flight (TOF) technique, which allows the separation of TPEs from background hot electrons [52–54]. This steradiancy/TOF combination was used in single-bunch synchrotron radiation TPE experiments, achieving a resolution of 1.6 meV (FWHM) with little contamination by hot electrons.

2.2.1. Penetration field technique

Hall et al. have recently applied the penetrating field technique in combination with an electron energy analysis for the detection of TPEs [23,54–56]. The application of this technique for TPE studies using synchrotron sources has yielded excellent results. The collection efficiency for TPEs formed at the photoionization region is optimized by a penetrating electrostatic field, which allows the repeller field for extracting the TPEs toward the electron detector to be minimized. Since background hot electrons that travel toward the detector are filtered by both the chromatic aberration of the electrostatic lens system and the energy analyzer, the problem caused by the transmission of hot electrons, as in using a steradiancy

analyzer, is greatly suppressed. As a result, the penetrating field technique is found to provide high resolution and better sensitivity in comparison to steradiancy-type electron spectrometers. When it is necessary to further suppress the hot electron background, the TOF analysis can also be combined with the penetrating field technique in a single-bunch synchrotron operation. The highest resolution demonstrated using the penetrating field technique in synchrotron measurements is ≈1.0 meV (FWHM)[55]. Since the best TPE resolution observed using the penetration field method was mainly limited by the VUV optical bandwidth, we expect that a higher TPE resolution can be achieved in the near future by employing a higher-resolution VUV source.

2.3. Photoelectron-photoion coincidence studies

As pointed out above, the AE measurements for polyatomic species using the photoionization mass spectrometric method are often affected by the hot band and kinetic shift effects, making the determination of the "true" AE ambiguous. In principle, the most reliable method for AE determinations is based on the analysis of the breakdown curves obtained in a photoelectron-photoion coincidence (PEPICO) experiment [57,58]. For a more detailed account of recent advances in PEPICO techniques and their applications for unimolecular dissociation studies, readers are referred to the review of Baer in the present volume.

2.3.1. TPE-photoion coincidence studies

The resolution of the PEPICO technique depends critically on the accompanying photoelectron method. The TPE-photoion coincidence (TPEPICO) scheme is the combination of the PIE and TPE spectroscopic methods for the detection of correlated mass-selected ions and TPEs [57–61]. The TPEPICO technique requires the continuous production of electron-ion pairs and is the preferred coincidence method when a tunable, continuous, or pseudo-continuous ionizing VUV light source is used. Since TPEs or ZEKEs are selected in a TPEPICO study, the internal energy for the molecular ion produced is thus equal to the difference between the photon energy and the IE for the molecule of interest. The TPEPICO technique has been successfully employed for studies of state- or energy-selected unimolecular dissociation dynamics and for measuring the TPE spectrum for a minor radical or size-selected cluster species produced in an impure radical or cluster source [62–66]. However, because of the hot-tail problem associated with TPE detection, most AE values obtained in previous TPEPICO studies are found to have uncertainties comparable to those of PIE measurements [4,5].

The successful application of the penetration field method for TPEPICO measurements has made possible the measurement of high-resolution TPE spectra for heterogeneous rare gas dimers, achieving resolutions of 2–3 meV [23]. As pointed out above, the penetration field method does not allow the use of an ion extraction field. In order to attain high ion-collection efficiency, the ion flight tube used in the penetrating field TPEPICO experiment is very short, which in effect sacrifices the TOF mass resolution. By nature of the design of the penetration field technique, its use in TPEPICO measurements is not expected to yield accurate kinetic energy release information for fragment ions.

2.3.2. TPE-secondary ion coincidence studies

As an extension of the TPEPICO technique, the TPE–secondary ion coincidence (TPESICO) method involves the correlated detection of TPEs and secondary ions formed in bimolecular collision processes [7,67–69]. This method has been demonstrated to be a general method for the study of state- or energy-selected ion-molecule reaction dynamics. As expected, the application of the TPESICO method for the study of bimolecular reactions is more difficult than that of the TPEPICO scheme for the investigation unimolecular dissociation processes. The successful application of the TPESICO method for state-selected ion-molecule reaction studies requires a very careful experimental consideration.

2.3.2.1. Signal-to-noise analysis

Below, we try to present a feasibility analysis of a TPESICO experiment. In a coincidence experiment concerning the selection of a vibronically excited ion

state, the ions of interest may represent a very small fraction of all the ions formed in the photoionization process at a particular photon energy. The essential feature of a coincidence experiment is that state-selected reactant ions arrive at the reaction region at a specific time with an uncertainty (full width) of $\Delta t'$ as measured with respect to the detection of corresponding TPEs. For a well-designed ion optics system, the $\Delta t'$ value can be made to have a small value of $\approx$50–150 ns, depending on the reactant ion mass and beam energy. Other ions formed in different internal states, which are not time correlated with the energy-selected photoelectron, are expected to arrive at the reaction region uniformly in time and, thus, appear as a uniform background in the coincidence TOF spectrum for the reactant ion. In a state-selected experiment using TPE, the ionization rate at the threshold (N_t) is of interest. The true coincidence rate C for state-selected reactant ions and false coincidence rate F for background ions arriving at the reaction region are related to N_t, the total ionization rate N, the electron transmission f_e, and the ion transmission f_i as given by Eqs. (3) and (4), respectively.

$$C = N_t f_e f_i, \tag{3}$$

$$F = (N_t f_e)(N f_i \Delta t') = N_t N f_e f_i \Delta t'. \tag{4}$$

If we assume that the reactions between reactant ions in different internal states and the neutral target molecules have identical cross section (σ), the true secondary ion coincidence rate (SC) and secondary false coincidence rate (SF) under thin target conditions can be calculated by Eqs. (5) and (6), respectively.

$$\mathrm{SC} = (N_t f_e f_i)(\sigma n l), \tag{5}$$

$$\mathrm{SF} = (N_t N f_e f_i)(\sigma n l)(\Delta t), \tag{6}$$

Here, Δt is the full width of the coincidence TOF peak for the product ion, which depends on scattering dynamics as well as the length l of the gas cell. The value for Δt is expected to be greater than that for $\Delta t'$. The S/N ratio of a PFI-PESICO experiment is thus predicted by Eq. (7).

$$\frac{S}{N} = \sqrt{\frac{N_t f_e f_i n l \sigma t}{1 + 2N\Delta t}}. \tag{7}$$

When reactant ions prepared by photoionization are not pure, the production rate (N_i) for the reactant ions of interest is $<N$. In these cases, the S/N ratio can be improved by using a reactant mass spectrometer, such as a quadrupole mass spectrometer (QMS), to select only reactant ions of interest. The S/N ratio achieved using a reactant QMS can be calculated by an equation similar to Eq. (7),, except that the term $2N\Delta t$ is replaced by $2N_i\Delta t$.

Referring to Eq. (7), a good coincidence experiment requires the minimization of the term $2N\Delta t$. Eq. (7) indicates that the S/N ratio for a TPESICO experiment is

$$\leq \sqrt{N_t f_e f_i n l \sigma t}.$$

This analysis shows that in a TPESICO study, it is essential to maximize f_e and f_i and to have a high sensitivity for PFI-PE detection to yield a high N_t value. Assuming typical values for N_t=1000 counts/s, f_e=0.1, f_i=0.6, $n=7\times10^{12}$ molecules/cm^3 (2×10^{-4} Torr), l=10 cm, and $\sigma=10^{-17}$ cm^2 (0.1 Å^2), we calculate

$$\mathrm{S/N} \leq 0.2054\sqrt{t}$$

To obtain an S/N=10, the time required is $\approx$0.65 hr.

2.4. Laser-based pulsed-field ionization studies

2.4.1. Pulsed-field ionization photoelectron measurements

Perhaps the most important development in photoelectron spectroscopy in the past 2 decades is the introduction of the laser-based pulsed field ionization (PFI)-photoelectron (PFI-PE) technique, which has been shown to achieve photoelectron energy resolutions close to the laser optical bandwidth [7–9,25,26]. The high resolutions achieved have allowed the measurements of rotationally resolved photoelectron spectra for many small molecules [8]. With the proper spectroscopic analysis and simulation, a rotational-resolved spectrum can in principle provide the definite

IE value for the molecule involved with an uncertainty limited only by the energy calibration [8,14]. Readers interested in this subject are referred to recent reviews [8,70,71]. The PFI-PE method is historically referred to in the literature as ZEKE spectroscopy [9]. The other name in use is ZEKE-PFI spectroscopy [9]. Since ZEKE spectroscopy originally stood for TPE spectroscopy, the use of ZEKE spectroscopy for PFI-PE detection is not appropriate.

Although the basic procedures for laser-based PFI-PE measurements were discovered in 1984 by Müller-Dethlefs, Sander, and Schlag [25], the detailed mechanism [26] involved was only suggested in 1988. This technique involves the detection of PFI-PEs formed in the delayed PFI of long-lived high-n ($n \geq 100$) Rydberg species initially formed by pulsed laser excitation. Because of the existence of a small stray electric field at the photoionization/photoexcitation (PI/PEX) region, background electrons produced by direct ionization and/or prompt autoionization can be effectively dispersed in a few hundred nanoseconds. As a result, the PFI-PE detection can be made free from background prompt electrons by delaying the application of the pulsed electric field for PFI by $\approx$1–5 μs with respect to the excitation laser pulse. We note that PFI-PEs are near ZEKEs formed slightly (a few cm^{-1}) below the true IE. The observed PFI-PE peak is lower than the true IE by the Stark shift (Δ) as predicted by the equation

$$\Delta = A\sqrt{F}\ \mathrm{cm}^{-1}, \tag{8}$$

where F is the magnitude of the pulsed field in Volts per centimeter and A is $\sim$6 for adiabatic ionization (where the molecule follows the lowest energy path) and 4 for diabatic ionization (where the molecule stays in one quantum level). Experiments show that the value for A lies in the range of 4–6. On the basis of the continuity of oscillator strength density, relative intensities for photoelectron bands observed in a PFI-PE spectrum are expected to be identical to those resolved in a TPE spectrum, provided that perturbations by nearby autoionizing states are ignored.

The understanding of Rydberg state properties relevant to PFI spectroscopy owes much to the initial work of Chupka [72]. The key requirement for the success of delay PFI-PE measurements is the long lifetimes for high-n Rydberg species prepared in optical excitation. Because of the small overlap of a Rydberg orbital wavefunction with low-n wavefunctions and the small energy gap to neighboring (high-n) levels, high-n Rydberg states are expected to have very long radiative lifetimes. Hence, radiative decay is not an important loss mechanism for high-n Rydberg states. However, autoionization of a neutral Rydberg species lying above the lowest IE can always occur by transferring sufficient energy from the ion core to the Rydberg electron. Based on the type of core energies transferred to the departing electron in molecular autoionization, the mechanisms involved can be classified as rotational, vibrational, and electronic autoionization. Simple consideration based on the atomic model predicts that the lifetime of a Rydberg state is proportional to n^3[41,42]. However, this prediction is found to be much too low compared to lifetimes observed in PFI experiments. The lifetime extension mechanisms have been a topic of intense investigation in the recent literature. It is generally accepted that the perturbation induced by stray electric fields or by electric fields arising from nearby prompt ions at the PI/PEX region is the mechanism for l- and m_l-mixings[73–76]. Since high-l states have nearly circular orbits and few interactions with the ion core, the lifetimes of high-l states are longer because they are more stable against autoionization (and predissociation, in the case of molecules). Because of dipole selection rules, the high-n Ryberg molecules initially formed by optical excitation should have low l quantum numbers. The l-changing mechanism, which leads to higher l states, can be induced by electrostatic fields of cylindrical symmetry (such as the stray field associated with the ion lenses). The m_l-mixing is believed to be induced by noncylindrical electrostatic fields caused by nearby prompt ions. The lifetime lengthening effect by m_l mixing is statistical in nature. The average lifetime for a statistical mixture of (l, m_l) states of the same n is predicted to scale as $n^{4.5}$, a prediction in accord with experimental observations.

2.4.2. PFI-photoion measurements

Instead of detecting the photoelectrons formed in the PFI of high-*n* Rydberg species, the same PFI process can be probed by detecting the PFI-photoions (PFI-PIs). Since both the internal energy and mass of a PFI-PI are known, the PFI-PI detection scheme is more specific and is equivalent to traditional PEPICO measurements employing a continuous or pseudo-continuous ionization source. Zhu and Johnson [27] reported the first PFI-PI measurement in 1991. They have named such measurements mass analyzed threshold ion (MATI) spectroscopy. For a detailed account on this topic, readers are referred to the recent review by Johnson [32].

It has been shown that the achievable energy resolutions for PFI-PE and PFI-PI measurements are similar and significantly higher than those obtainable in conventional TPE measurements. Similar to PFI-PE measurements, the PFI-PI detection scheme requires the dispersion of background prompt ions from PFI-PIs by the TOF separation. Since this is more difficult compared to the dispersion of background prompt electrons in PFI-PE detection, fewer PFI-PI systems than PFI-PE systems have been reported. The common strategy for PFI-PI measurements is to apply a small dc (direct current) field followed by a delayed electric field for PFI. Since the trajectories for neutral high-*n* Rydberg molecules are not affected by the dc electric field, the dc field serves as a separation field and has the function of deflecting the prompt ions in such a way that they are slightly separated from the high-*n* Rydberg molecules in the ion source. The PFI-PIs produced by a delay PFI field can thus be spatially separated from the prompt ions. This separation in the ion source allows the prompt ions and PFI-PIs to gain different acceleration during the ion extraction process, which in turn makes it possible for the PFI-PIs to be distinguished from the background prompt ions by TOF detection. The dc field used also has the effect of depleting the population of very high *n* Rydberg states, along with lengthening the lifetime for the (intermediate) high-*n* Rydberg level. However, the application of too high a dc field often reduces the population of high-*n* Rydberg states, resulting in a devastating loss of the PFI-PI signal.

When using the TPESICO method for the preparation of state-selected reactant ions for ion-molecule reaction studies, correlated ions (ions in specific internal states of interest), together with uncorrelated ions (i.e., false ions formed in different ion states), are usually sent into the reaction region to react with the neutral reactants. This is a major disadvantage for the application of the TPESICO method for state-selected reaction/ion-molecule reaction studies because it necessarily involves a subtraction procedure. This would significantly reduce the S/N ratios of cross-section data, especially in the case where the reaction cross sections for false ions are greater then those for the correlated reactant ions. The application of the PFI-PI method would avoid this problem. Furthermore, Eq. (7) shows that the *S*/*N* for a PEPICO measurement is affected by the electron transmission function f_e, which usually has a value of $\leq$0.5. The *S*/*N* for a PFI-PI experiment does not involve the f_e factor and should be significantly higher than that for a PEPICO study. This comparison of *S*/*N* analyses for ion–molecule reaction studies using the PEPICO and PFI-PI methods also applies to photodissociation studies of state-selected ions.

Efforts have been made to utilize the VUV laser PFI-PI scheme for the preparation of state-selected reactant ions for ion-molecule reaction dynamics studies [77,78]. Because of the high resolution achieved in PFI-PI studies, it should be possible to prepare rotationally selected reactant ions using this method. Further developments in the application of PFI-PI schemes for the study of ion–molecule reaction dynamics and photodissociation dynamics are to be anticipated.

2.4.3. PFI–ion pair measurements

Adding to the PFI-PE and PFI-PI schemes in PFI experiments, the formation of ion pairs has been demonstrated in PFI experiments by Hepburn and coworkers [33,34]. This PFI–ion pair (PFI-IP) method is originally referred as the threshold ion pair production (TIPP) spectroscopy. The formation of ion pairs as induced by a Stark dc field was first reported by

Pratt and coworkers in an article concerned with the ion pair formation of H_2[79]. The experimental arrangement for PFI-IP detection is similar to that employed for PFI-PI measurements. That is, the discrimination of background prompt ions is achieved by a separation dc electric field maintained at the PI/PEX region. The electric field pulse for inducing the formation ion pairs is applied after an appropriate delay with respect to the excitation laser pulse.

The interaction potential for an ion pair state is analogous to that for a high-*n* Rydberg state and is Coulombic in nature. Thus, the ion pair potential is expected to sustain an infinite number of vibrational levels, similar to an infinite number of Rydberg levels supported by an electron-ion core potential. In addition to spectroscopy information for the ion pair state, the determination of the threshold for the ion pair formation can be used for determining the D_0 value for a neutral molecule provided that the electron detachment energy for the anionic fragment is known. The electron detachment energy is equal to the electron affinity (EA) for the reverse process. A good database exists for EA of many simple molecular species, resulting from extensive laser photodetachment studies in the past decades [5]. The PFI-IP technique has been successfully applied to the study of several diatomic and triatomic molecules [33,34]. These experiments have provided highly accurate D_0 values for these molecules. Generally, the FCFs for the formation of ion pair states from the ground neutral state of a neutral molecule are poor. This may limit the number of ion pair systems that can be examined by this method. In principle, the same information obtained in a PFI-IP study can also be gained in a high-resolution coincidence study, where correlated anionic and cationic fragments induced by PFI are measured.

2.4.4. Photoinduced Rydberg ionization measurements

As indicated above, excited molecules in high-*n* ($n \geq 100$) Rydberg states formed by pulsed-laser excitation are found to have extended lifetimes in the range of $\approx$1–10 μs. These lifetimes are sufficiently long to allow further excitation of the high-*n* Rydberg species by a second laser. A long-lived high-*n* Rydberg molecule can be considered to comprise an ion core and a weakly interacting electron in a high-*l* Rydberg state with a near spherical orbit. On the absorption of the second laser photon by the ion core, an excited high-*n* Rydberg level with an excited ion core is formed. The autoionization lifetime of such an excited Rydberg state is likely shorter than that of the high-*n* Rydberg level before photoexcitation. By detecting the ions thus produced as a function of the second excitation laser frequency, we essentially produce a high-resolution absorption spectrum of the ion. This two-color ionization scheme is referred as photoinduced Rydberg ionization spectroscopy (PIRI) in the literature [28–32]. To prepare high-*n* Rydberg species for PIRI measurements, the first excitation laser should be a UV or a VUV laser.

As long as the quantum defects for the lower and upper Rydberg states are similar, we expect that the PIRI spectrum is similar to that of the cation. In PFI experiments, the energy resolution is limited by the *F* value of the Stark field (see Eq. [8]). However, the PIRI method does not require a PFI field. The energy resolution for PIRI measurements should be governed basically by the optical resolution of the second laser, the quantum defect spread, and natural line widths. Thus, the PIRI method is expected to provide better resolution than those of PFI-PE and PFI-PI measurements in favorable cases. The resolution capability for PIRI measurements has not been tested because the molecules studied to date have natural line widths that are greater than rotational spacings [32].

In principle, there is no limit on the frequency of the second excitation laser so long as autoionization is induced by such an excitation. Johnson and coworkers have performed PIRI measurements by excitation of the ion core to rovibrational levels of an excited electronic state using a dye laser in the visible frequency range [28–31]. Recent PIRI measurements have also been successfully made using infrared lasers, resulting in the excitation of the ion core in vibrationally excited levels of the ground electronic state [80].

Since the introduction of the PFI methods, the list of molecules investigated by PFI-PE and PFI-PI

schemes has been expanding steadily, yielding a growing list of IE values with uncertainties $\leq$1 meV (8 cm^{-1}). The rotationally and/or vibrationally resolved spectra obtained for these molecules have also provided a wealth of spectroscopic data for the corresponding cations. However, the full potential of the laser-based PFI techniques have not been realized because of the limited tunable range accessible by lasers and the time-consuming procedures involved for laser VUV generation. The real impact of these PFI techniques on chemistry requires a high-resolution, broadly tunable VUV source.

2.5. Synchrotron-based PFI studies

In the past few years, we have established a high-resolution, broadly tunable VUV source at the Chemical Dynamics Beamline of the Advanced Light Source (ALS) [16–22]. However, the (pulsed) laser-based PFI-PE technique has traditionally required a delay of $\approx$1–3 μs for the dispersion of prompt background electrons [8,25,26]. Thus, this approach is not directly applicable to PFI-PE measurements using synchrotron radiation, which is essentially a continuous light source. We have developed a novel synchrotron-based PFI-PE scheme overcoming the delay requirement and have attained resolutions of 2–5 cm^{-1} (FWHM)[20]. Recently, we have improved the PFI-PE resolution and prompt electron discrimination by introducing the TOF detection scheme [19]. This method has achieved a PFI-PE resolution of 1 cm^{-1} (FWHM) at 12.123 eV, which is similar to that attained in laser-based PFI-PE studies. The ease of tunability of this ALS synchrotron source has made rotationally resolved PFI-PE measurements for many molecules a routine operation [81–98]. The high sensitivity of the photoelectron-photoion apparatus has allowed the measurements of rotationally resolved photoelectron spectra of many diatomic molecules, covering vibrational levels up to the dissociation limits of the corresponding diatomic ions [90–92,95,96].

Recently, we have developed a synchrotron-based PFI-PE-photoion coincidence (PFI-PEPICO) method, which makes possible the internal state selection for cations at a resolution of 0.6 meV (4.8 cm^{-1}, FWHM) limited only by the resolution of PFI-PE measurements [21]. By employing this PFI-PEPICO method, together with the supersonic beam technique for rotational cooling of gas samples, we show that the accurate AE at 0 K can be determined unambiguously by the disappearance energy of the parent ion. As a result, D_0 values for many small neutrals and cations have been determined with unprecedented precision using the PFI-PEPICO method [99–102]. These accurate D_0 values, along with accurate IE values obtained in PFI-PE measurements, are expected to serve as new standards and provide an impetus for the further improvement of ab initio quantum computation models, such as the Gaussian-2 and Gaussian-3 procedures [36,37,103,104]. Most recently, we have demonstrated a synchrotron-based PFI-PI detection scheme [22]. This method shows promise to become a general method for state-selected reactant ion preparations for the study of ion–molecule reaction dynamics and ion photodissociation dynamics. Using selected examples, we will briefly describe these new developments below.

2.5.1. High-resolution VUV synchrotron facility of the Chemical Dynamics Beamline

The high-resolution VUV facility of the Chemical Dynamics Beamline consists of a 10-cm period undulator (U10), a gas harmonic filter [105], a 6.65-m Eagle scanning monochromator, and a multipurpose photoelectron-photoion apparatus [16–22].

Synchrotron radiation arises because of motion of light elementary charged particles, such as electrons, that approach the speed of light and are deflected in their trajectories by magnets. The radiation from an electron storage ring, such as the ALS, is given off in the forward direction and is observed in the laboratory as a small cone along the trajectory of the electrons. The ALS radiation is 99% polarized in the horizontal plane perpendicular to the direction of the photon beam [18]. Compared to second-generation synchrotron light sources, the ALS is a third-generation light source, which provides higher photon intensities and smaller spot sizes. The tighter focusing of the electron bunches in third-generation synchrotron sources al-

lows a more effective coupling of insertion devices, such as undulators, to further magnify the photon intensities. An undulator is installed in the straight sections of the storage ring and consists of a periodic array of permanent magnets, which force the electrons to oscillate with a period of a few centimeters over a length of several meters. Since each wiggle emits synchrotron radiation in the same forward direction, the undulator has the effect of amplifying the synchrotron light intensity. Because of the interference effect, an amplification factor up to the square of the number of periods can be achieved using an undulator. As for the U10 undulator associated with the Chemical Dynamics Beamline, the number period is 43. The fundamental or first harmonic of the U10 undulator radiation has a VUV bandwidth of ≈2.5% and a photon intensity of $\approx 10^{16}$ photons/s [18].

The ALS storage ring is capable of filling 328 electron buckets in a period of 656 ns. Each electron bucket emits a light pulse of 50 ps with a time separation of 2 ns between successive bunches [16,18]. In each storage period, a dark gap of 16–144 ns consisting of 8–72 consecutive unfilled buckets exists for the ejection of cations from the ring orbit. Thus, in the multibunch mode, the synchrotron ring has 256–320 electron bunches in its orbit, corresponding to a repetition rate of 390–488 MHz. The ALS storage ring also operates in the two-bunch mode, where the time separation between successive bunches is 328 ns, corresponding to the repetition rate of 3.04 MHz. Because of the high repetition rate of the ALS radiation, it can be regarded as a pseudo-continuum light source.

Using the U10 with the synchrotron ring operated at 1.5 GeV electron energy, the first order (or fundamental) of the undulator harmonics can be tuned in the photon energy range from 8 to 30 eV [16,18]. Harmonics that appear at energies higher than the first order (or fundamental) harmonic of the undulator spectrum can give rise to a major source of background in a photoionization experiment. Thus, a rare gas harmonic filter was designed to suppress these higher harmonics [105]. Using a rare gas, He, Ne, or Ar, as the filter gas, higher harmonics at photon energies higher than the IE, 24.59, 21.56, or 15.76 eV, respectively, can be effectively suppressed.

The filtered undulator VUV beam, which consists predominantly of the first undulator harmonic, was directed into the 6.65-m monochromator, where the VUV beam was dispersed before refocusing into the PI/PEX region of the photoelectron-photoion apparatus by a toroidal mirror. The VUV photon spot size at the PI/PEX region is estimated to be 0.3 mm in width and 0.2 mm in height. The 6.65-m monochromator is equipped with a 4800 lines/mm grating and has demonstrated the resolving power of $E/\Delta E$ 72,000–100,000 in the VUV range of 6–30 eV [17,19], where E and ΔE represent the photon energy and photon energy bandwidth, respectively. This resolving power is close to that achieved in common VUV lasers. Depending on the resolution and grating used, the VUV photon intensity observed varies in the range of 10^{-9} to 10^{12} photons/s [18].

For PFI-PE measurements, the photon energy calibration was achieved using the known IEs of the rare gases (He, Ne, Ar, Kr, and Xe) and/or diatomic molecules (O_2, N_2, NO, and H_2) measured under the same experimental conditions [16,18]. This calibration scheme assumes that the Stark shifts for the molecules of interest and the calibration gases are identical. On the basis of previous experiments, we estimate that the energy calibration has an uncertainty of ± 0.5 meV [86,90].

Fig. 1 depicts the schematic diagram of the photoelectron-photoion spectrometer, showing the lens arrangement for electron and ion TOF detection [21]. Typical voltages applied to the lens E1-E5 and I1-I11 associated with the electron and ion TOF spectrometers, respectively, are also shown in the figure. Two sets of dual microchannel plates (MCP) were used for electron and ion detection. The midpoint between I1 and E1 defines the PI/PEX center. The electron TOF spectrometer has been modified from the one used in previous experiments [20]. The main difference was that the hemispherical analyzer had been removed and only a steradiancy analyzer was used as the electron TOF spectrometer, as shown in Fig. 1.

The gas sample is usually introduced into the PI/PEX region as a skimmed supersonic beam pro-

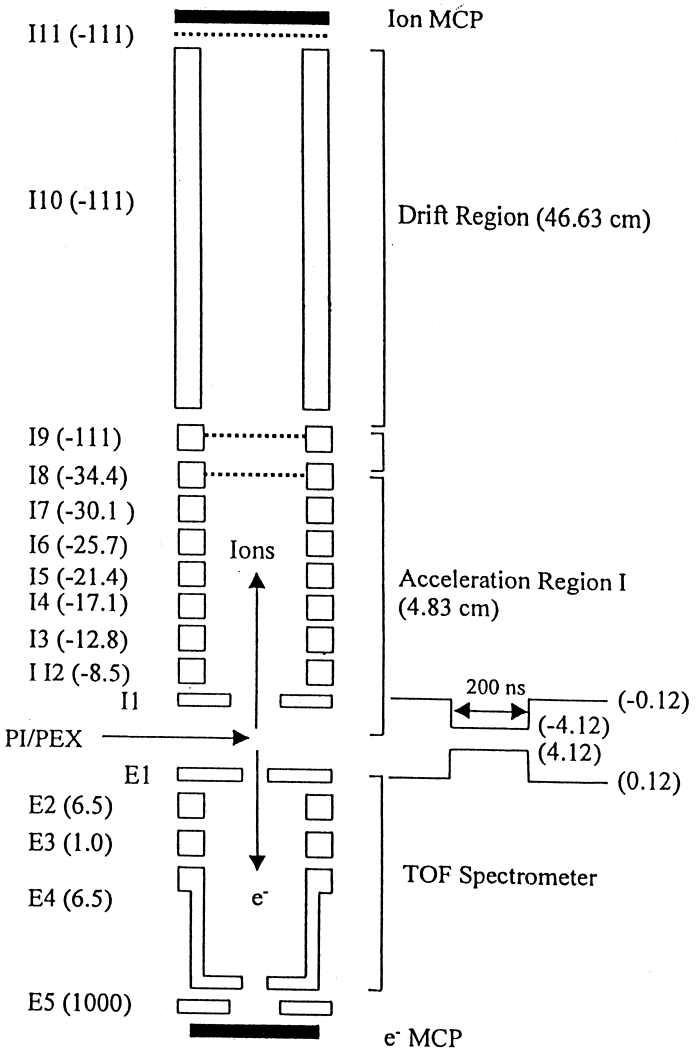

Fig. 1. Schematic diagram for the PFI-PEPICO spectrometer [21]. The electron lenses and ion lenses are labeled as E1-E5 and I1-I11, respectively. The PI/PEX center is defined by the centered between I1 and E1. Electrons and ions are detected using MCP detectors. The ion TOF spectrometer consists of acceleration region I, acceleration region II, and a drift region with the distances of 4.83, 0.54, 46.63 cm, respectively. Typical voltages applied to individual lenses are given in parentheses.

duced in a two-stage or three-stage differentially pumping arrangement [16]. The sample can also be introduced as an effusive beam at 298 K through a metal orifice with a diameter of 0.5 mm and a distance of 0.5 cm from the PI/PEX region [87].

2.5.2. PFI-PE measurements

The synchrotron-based PFI-PE schemes make use of the dark gap—a short time lapse in every synchrotron ring period where no synchrotron light is emitted. Two schemes [19,20] have been developed and successfully applied to PFI-PE measurements of many atomic and molecular systems. The earlier method [20] involves the used of an electron spectrometer, which is equipped with a steradiancy analyzer and a hemispherical energy analyzer arranged in tandem. Using such an electron spectrometer, we have previously shown that PFI-PEs can be detected with little

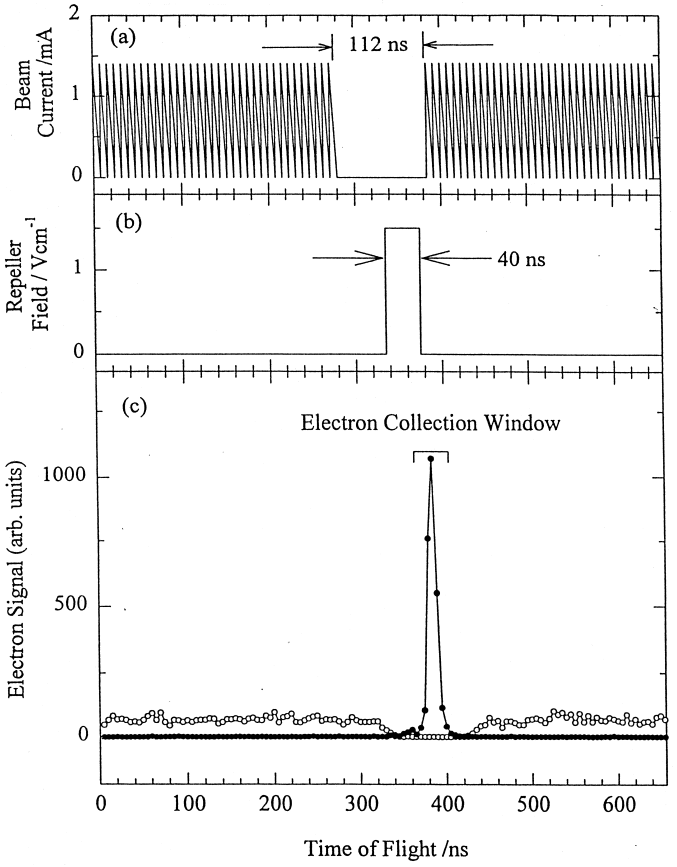

Fig. 2. The timing structures for (*a*) the pattern of VUV light bunches emitted in the ALS multibunch mode; (*b*) the electric field pulses applied to lens E1 (see Fig. 1); and (*c*) the electron TOF spectra of PFI-PEs (*filled circles*) as observed at the $Ar^+(^2P_{3/2})$ PFI-PE peak and hot or prompt electrons (*open circles*) as observed at the Ar(11s′) autoionizing state [19].

background from prompt electrons after only an 8-ns delay with respect to the beginning of the dark gap. The most recent PFI-PE scheme [19] employs the TOF method for the selection of PFI-PEs and is superior to that using the electron spectrometer.

Here, we use Ar as the gas sample to illustrate the TOF PFI-PE selection scheme [19]. In this scheme, a dc field of 0.2 V/cm was applied to the PI/PEX region for pushing hot electrons arising from autoionization and direct ionization toward the electron detector. We note that a dc field has the effect of inducing the ionization of high-*n* Rydberg states and, thus, lowering the PFI-PE intensity. However, experiments show that the decrease of the PFI-PE signal caused by field-induced ionization is minor for a dc field of $\leq$0.2 V/cm.

Fig. 2(a) shows the pattern of the ALS light pulses in a typical multibunch operation. The two shaded areas represent stacks of uniformly spaced synchrotron microlight bunches (width=50 ps, separation=2 ns) [19. For clarity, the 112-ns dark gap is shown centered in the 656-ns ring period in Fig. 2(a). Following a delay of some 20 ns with respect to the beginning of the dark gap, an electric field pulse (width=40 ns) in the range of 0.3–1.5 V/cm was applied to the PI/PEX region [see Fig. 2(b)] [19]. The frequency of the electric field pulse for the PFI was 1.53 MHz, which is consistent with the ring period. When the photon energy was set to coincide with the $Ar^+(^2P_{3/2})$ PFI-PE peak at 15.7596 eV, the observed TOF spectrum [Fig. 2(c), solid circles) for PFI-PEs was found to exhibit a single peak with a full width of

≈40 ns [Fig. 2(c)] [19]. We note that the time zero of the TOF spectra shown in Fig. 2(c) corresponds to the triggering pulse provided by the ALS, the position of which is arbitrary. Partly because of the small VUV spot size at the PI/PEX region, the observed TOF peak for PFI-PEs was narrow. We note that the observed full width of 40 ns is equal to the width of the PFI pulse. This observation indicates that the PFI-PEs formed within 40 ns during the application of the Stark pulses were highly monoenergetic with little dispersion as they traveled from the PI/PEX region to the electron detector. No prompt electrons can be observed at 15.7596 eV because this energy is below the IE of Ar. It can be seen from the comparison with the positions of the Stark pulse [Fig. 2(b)] and the TOF peak for PFI-PEs that the TOF for PFI-PEs from the PI/PEX region to the electron MCP detector is ≈50 ns. As the photon energy was slightly increased above the IE for the formation of $Ar^+(^2P_{3/2})$, the single TOF peak for PFI-PEs disappears and an electron TOF spectrum for prompt electrons resembling the synchrotron orbit pattern was observed as these electrons are extracted continuously by the small dc field. The electron TOF spectrum [Fig. 2(c), open circles] observed using a 1.5-V/cm Stark pulse at 15.7655 eV corresponding to the position of the Ar(11s′) autoionizing Rydberg state is also shown in Fig. 2(c). In this spectrum, a small electron signal caused by prompt electrons was observed uniformly in time except in a window of ≈110 ns corresponding to the width of the dark gap, where essentially no electrons were formed.

The location of the PFI-PE peak in the TOF spectrum depends on the height of the Stark pulse and the delay with respect to the beginning of the dark gap. These parameters were adjusted such that the TOF peak for the PFI-PEs fell in the middle of the 112-ns window where no hot electrons were observed and, thus, achieved a clear separation of prompt electrons from PFI-PEs. As a result, PFI-PEs can be easily detected free from background prompt electrons by setting a gate with a width corresponding to the width of the TOF peak for PFI-PEs [Fig. 2(c)] [19].

The previous PFI-PE detection scheme using a hemispherical energy analyzer requires a sufficiently high PFI field pulse for attaining a high electron transmission [20]. The relatively high Stark pulse required also limits the attainable PFI-PE resolution. The transmission of PFI-PEs in this TOF scheme does not have a strong dependence on the applied pulsed electric field. Fig. 3(a) and 3(b) shows the PFI-PE bands of $Xe^+(^2P_{3/2})$ and $Ar^+(^2P_{3/2})$, respectively, measured using the TOF selection scheme .[19] The pulsed field used in this measurement was ≈0.3 V/cm. The Gaussian fit to these PFI-PE spectra reveals a resolution of 1.0 cm^{-1} (FWHM) for the $Xe^+(^2P_{3/2})$ band at 12.123 eV and 1.9 cm^{-1} (FWHM) for the $Ar^+(^2P_{3/2})$ band at 15.760 eV. These resolutions are more than a factor of two better than the best resolutions recorded for these PFI-PE bands in previous ALS experiments [20] and are closer to the best resolution (0.3 cm^{-1}, FWHM) reported [106,107] using laser PFI-PE techniques.

The rotationally resolved PFI-PE band for $H_2^+(X^2\Sigma_g^+, v^+=0)$ obtained using the TOF scheme and the hemispherical energy analyzer [20] are compared in Fig. 4(a) and 4(b), respectively [19]. The positioning of rotational transitions (N^+, J 178) from rotational J″ levels for H_2 to rotational N^+ levels for H_2^+ are marked in these figures. The resolution of the spectrum shown in Fig. 4(a) is clearly better than that of Fig. 4(b). The spectrum of Fig. 4(b) is significantly contaminated by nearby strong autoionizing resonances [108]. Nearly all the background peaks originating from strong autoionizing states seen in Fig. 4(b) are suppressed in the spectrum of Fig. 4(a). We estimate that the background electron suppression achieved using the TOF PFI-PE selection scheme is ≈10 times better than that observed using a hemispherical analyzer for PFI-PE detection.

2.5.3. PFI-PEPICO measurements

The PFI-PEPICO experiment requires the coincidence detection of PFI-PE and PFI-photoion with high efficiencies [21]. In this scheme, a dc field of ≤0.20 V/cm was applied across the PI/PEX region as in the PFI-PE detection [19]. The application of a PFI electric field pulse (height=7.0 V/cm, width=200 ns) was delayed by ≈10 ns with respect to the beginning

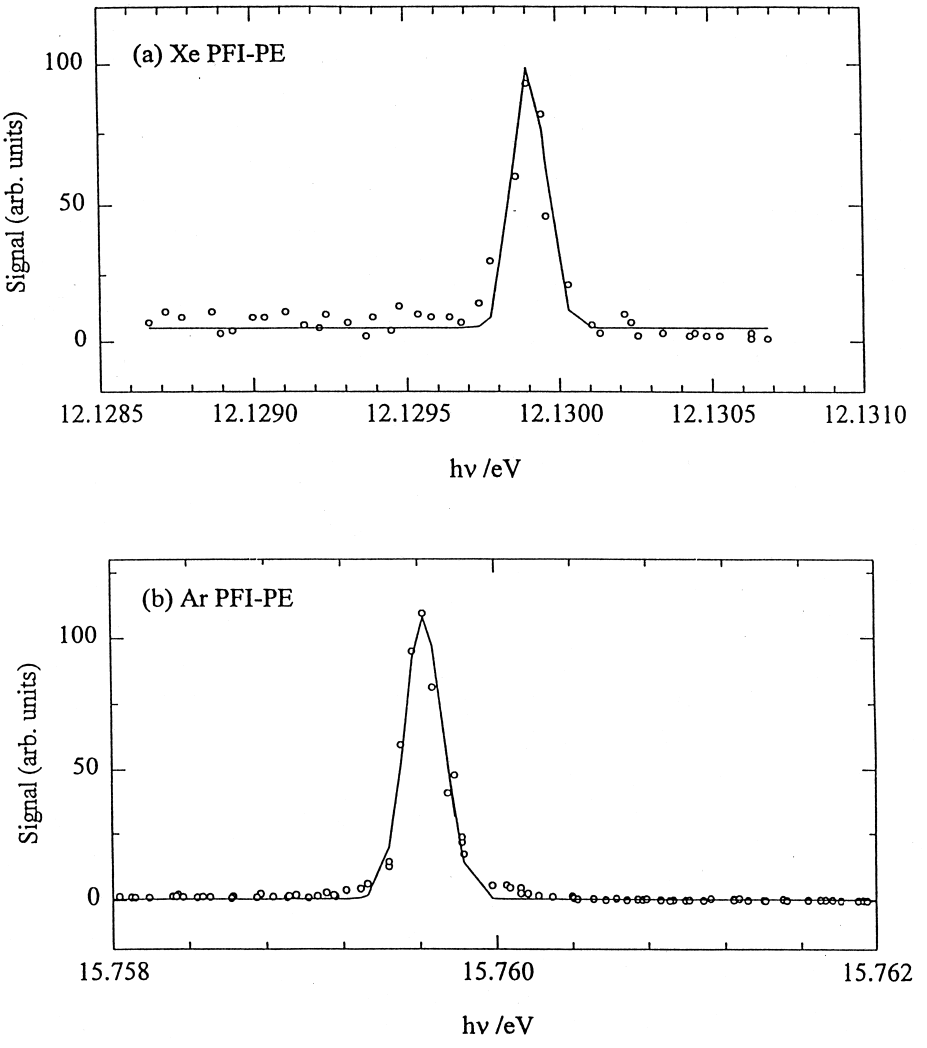

Fig. 3. (*a*) PFI-PE band for $Xe^+(^2P_{3/2})$ (*open circles*) obtained using a pulsed field of 0.3 V/cm [19]. A Gaussian fit obtained using a least-squares fit is also shown (*line*), revealing a FWHM maximum of 1.0 ± 0.2 cm^{-1}. (*b*) Experimental PFI-PE band for $Ar^+(^2P_{3/2})$ (*open circles*) obtained using a pulsed field of 0.3 V/cm [7]. A Gaussian fit obtained using a least-squares fit is also shown (*line*), revealing a FWHM of 1.9 ± 0.3 cm^{-1}. The 4800 lines/mm grating was used. The monochromator entrance/exit slits are set at 30/30 μm for both (*a*) and (*b*), corresponding to a nominal wavelength resolution of 0.0096 Å (FWHM).

of the 112-ns dark gap. We note that this same electric field pulse also serves to extract the PFI-PIs toward the ion detector. By comparing the coincidence rate with the PFI-PE and ion detection rates, we estimate the collection efficiencies for PFI-PE and PFI-PI to be 7.3 and 19.3%, respectively, at the PFI-PEPICO peak for $Ar^+(^2P_{3/2})$. The use of a relatively high pulsed electric field, on one hand, makes this PFI-PEPICO scheme more sensitive. On the other hand, it also limits the achievable PFI-PEPICO resolution to ≈1.0 meV (FWHM). The PFI-PEPICO experiments described here, unless specified, were performed using this scheme.

The highest PFI-PE resolution achieved so far involved the use of a shaped pulse for PFI and ion extraction [21]. The shaped pulse consists of a low field pulse (<1 V/cm, duration ≈20–40 ns) for PFI immediately followed by a higher pulse (>7 V/cm,

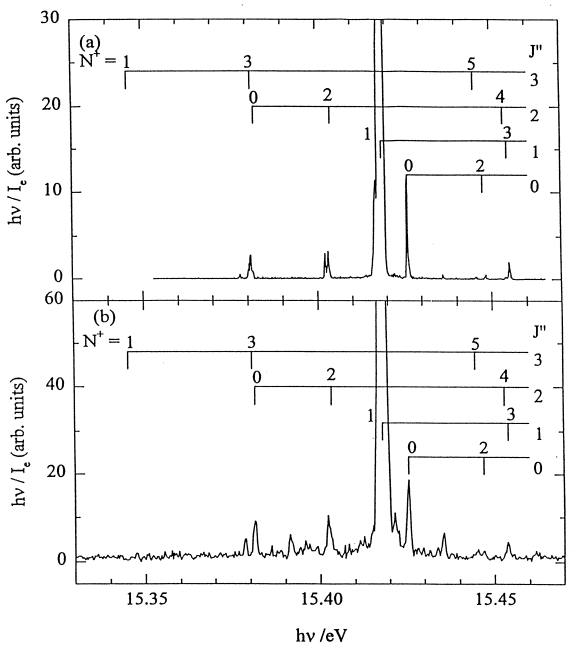

Fig. 4. PFI-PE spectrum for $H_2^+(X^2\Sigma_g^+, v^+=0)$ recorded (*a*) using electron TOF analysis with a 0-V/cm dc field, and a 1.50-V/cm pulsed field across the interaction region [19]. The 4800-lines grating was used. The monochromator entrance/exit slits are set at 10/10 μm, corresponding to a nominal resolution of 0.0064 Å (FWHM), (*b*) using a hemispherical and steradiancy analyzer in tandem and a 0.67 V cm^{-1} pulsed field at a nominal wavelength resolution of 0.048 Å (FWHM) [8].

duration ≈150 ns) for ion extraction. By collecting only PFI-PEs from the low field pulse, the resolution is expected to be higher than that obtained in the above scheme, where a 7-V/cm PFI pulse is used. An important experimental consideration is that the PFI-PEs formed by PFI because of the low field pulse must exit the PI/PEX region before the employment of the high field pulse. As the PFI-PEs enter the electron TOF spectrometer, they are shielded from the high field pulse by the grid located at the aperture of lens E1 (see Fig. 1). Thus, the high field pulse for ion extraction would not disturb the TOFs of PFI-PEs produced by the low field pulse. Fig. 5 compares the PFI-PE (open circles) and PFI-PEPICO (solid circles) bands for $Ar^+(^2P_{3/2,1/2})$ obtained using the shaped-pulse scheme [21]. These spectra were obtained using a 0.5-V/cm low field pulse (duration ≈40 ns) followed by a 7-V/cm high field pulse (duration ≈150 ns). The shaped pulse used is shown in the inset of Fig. 5. The Gaussian fit to the $Ar^+(^2P_{3/2})$ and $Ar^+(^2P_{1/2})$ bands gives experimental resolutions of 0.5–0.6 meV (FWHM). The PFI-PEPICO intensity is ~25% of the PFI-PE intensity, indicating that good collection efficiencies were achieved for both PFI-PEs and PFI-photoions. The shaped pulse basically solves the dilemma of achieving a high photoelectron resolution (requires a low electric field pulse) and a high ion transmission (requires a high electric field pulse).

Assuming that a gaseous sample with an average center-of-mass translational energy E_{cm}, as characterized by a translational temperature T, is photoionized and sampled by a TOF mass spectrometer, we expected to observe a TOF peak with a full-width Δt according to the prediction [21,22]

$$\Delta t = \sqrt{\frac{8mE_{cm}}{(qF)^2}}. \quad (9)$$

Here, m is the ion mass, F is the electric field at the PI/PEX region, and q is the elementary charge. The Δt value (full width) of the TOF peak is simply determined by the turnaround time of ions moving away from the ion TOF detector. Eq. (9) predicts that the TOF peak width for PFI-PEs is expected to be very narrow because of the low electron mass. The electron TOF spectrum of Fig. 2(c) confirms the latter expectation. We compare in Fig. 6 the PFI-PEPICO spectra for $Ar^+(^2P_{3/2})$ observed using a supersonic beam (upper spectrum) and an effusive beam (lower spectrum), respectively, to introduce the Ar sample [22]. The upper TOF spectrum exhibits a sharp peak (FWHM≈100 ns), which can be attributed to Ar^+ formed by photoionization of Ar in the supersonic beam with an E_{cm} corresponding to a translational temperature of ≈20 K. In addition to the sharp TOF component, the upper TOF spectrum is found to have a broad base, which can be attributed to Ar^+ ions produced by photoionization of thermal (298 K) ambient Ar background in the PI/PEX region. That is, these ions have an E_{cm} corresponding to 298 K. This conclusion is supported by the comparison with the effusive TOF spectrum (lower spectrum) in Fig. 6,

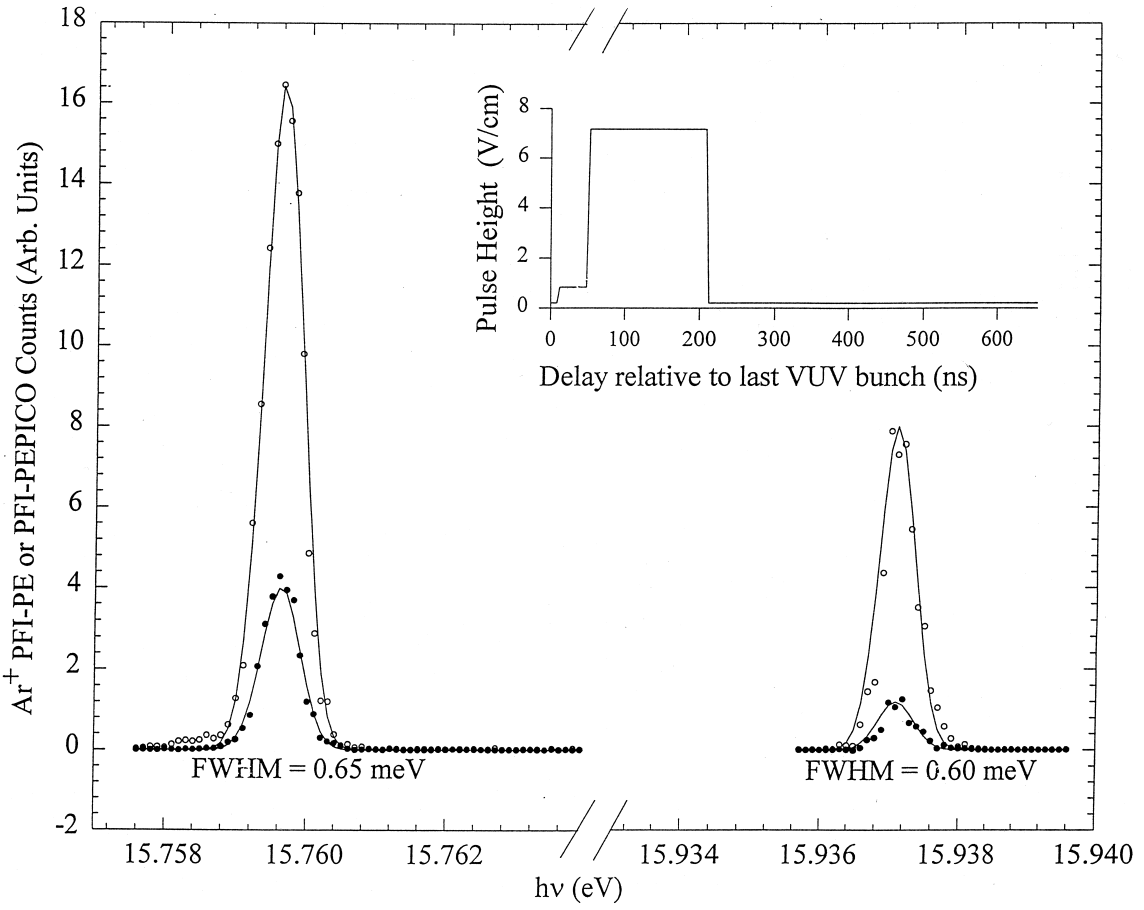

Fig. 5. Comparison of the PFI-PE (*open circles*) and PFI-PEPICO (*solid circles*) bands for $Ar^+(^2P_{3/2,1/2})$ obtained using the shaped pulse coincidence scheme [21]. The shaped pulse is shown in the inset. It consists of a 0.5-V/cm low field pulse (duration=40 ns) followed by a 7-V/cm high field pulse (duration=150 ns). The Gaussian fit to these bands yields a resolution of 0.6 meV (FWHM) for both the PFI-PE and PFI-PEPICO bands.

where the intensity of the latter spectrum has been normalized to that of the broad component of the cold TOF spectrum. A magnified view comparing the base for the upper TOF spectrum and the effusive TOF spectrum is depicted in the inset of Fig. 6. The effusive TOF peak is found to have a FWHM of ≈700 ns. The complex structure observed for the effusive TOF peak mostly results from the pseudocontinuous nature of the ion extraction. Simulation shows that the extraction of Ar^+ from the ion source, that is, the region defined by I1 and E1, requires several PFI-extraction field pulses. On the basis of the relative intensities for the narrow and broad TOF components, we estimate that the Ar sample observed consists of 85% of cold Ar in the supersonic beam and 15% thermal background Ar in the photoionization chamber. This ratio of 85 : 15 for the cold and thermal Ar is roughly consistent with the estimated number densities for the Ar supersonic beam and thermal background Ar at the PI/PEX region. In addition to providing this estimate for the cold/thermal ratio for Ar, this experiment shows that in a PFI-PEPICO study of a dissociative photoionization reaction, it is possible to distinguish the dissociation of cold ions from that of thermal background ions based on their TOF profiles.

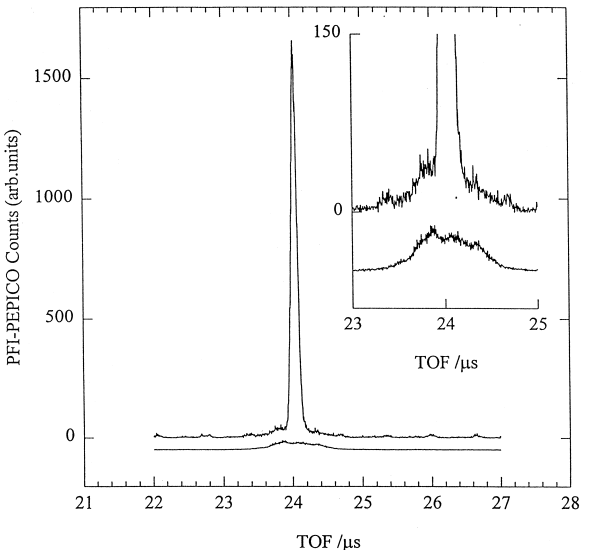

Fig. 6. PFI-PEPICO TOF spectra for $Ar^+(^2P_{3/2})$ obtained using an Ar supersonic beam sample (upper spectrum, translational temperature≈20 K) and an effusive Ar beam (lower spectrum, temperature=298 K) [22]. The intensity of the 298 K spectrum has been normalized to the broad component of the 20 K spectrum. The inset shows a magnified view, comparing the 298 K spectrum with the broad component of the 20 K spectrum.

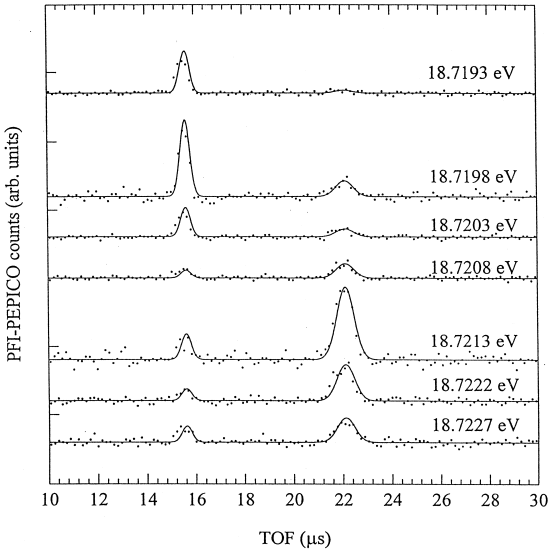

Fig. 7. Background-subtracted PFI-PEPICO TOF spectra for O^+ and O_2^+ from O_2 at 18.7193–18.7227 eV obtained using an effusive O_2 beam [21].

To illustrate the merits of the newly developed PFI-PEPICO technique for state-selected ion dissociation studies and accurate energetic measurements for ion and neutral species, we have summarized the results of the PFI-PEPICO studies on O_2 and CH_4 below [21,99]

2.5.3.1. Rotational-state-selected dissociation study of $O_2^+(b^4\Sigma_g^-, v^+=4)$

The lowest dissociation threshold for O_2^+ is known to occur just below $O_2^+(b^4\Sigma_g^-, v^+=4, N^+=9)$ [109–112]. Since the thermal O_2 sample promotes the populations of $N^+\geq 9$ rotational levels, which are responsible for the formation of O^+ fragments in the PFI-PEPICO measurement, we have examined in detail the branching ratios for O^+ and O_2^+ from O_2 in a PFI-PEPICO TOF experiment using an effusive O_2 sample. We have obtained PFI-PEPICO TOF spectra in the energy region of 18.7129–18.7253 eV at an energy increment of 0.5 meV [21]. Selected TOF spectra measured at photon energies of 18.7193–18.7227 eV are depicted in Fig. 7. The resulting breakdown data are plotted in Fig. 8(a), where the solid circles represent the branching ratios of O^+ and the solid squares are those for O_2^+. At a given photon energy in the breakdown diagram, the sum of the branching ratios for O^+ and O_2^+ is normalized to 1.0.

Fig. 8(b) shows the PFI-PE band for $O_2^+(b^4\Sigma_g^-, v^+=4)$, together with its simulation [21]. The marking of the $\Delta N=N^+-N''=-2$, 0, and +2 (or O, Q, and S, respectively) rotational branches is also shown in Fig. 8(b). Here N^+ and N'' are the rotational quantum numbers for O_2^+ and O_2, respectively. We note that the numbers marked in Fig. 8(b) are N'' values. The simulation allows the estimation of populations for the N^+ levels. The dashed line of Fig. 8(b) shows the population of $O_2^+(b^4\Sigma_g^-, v^+=4, N^+<9)$, which is expected to produce stable parent O_2^+ ions.

Our previous lifetime measurements for excited high–Rydberg states of O_2 ($O_2^*[n]$) converging to the dissociative $O_2^+(b^4\Sigma_g^-, B^2\Sigma_g^-$, and $c^4\Sigma_u^-)$ states show that prompt dissociation of $O_2^*(n)$ occurs to produce $O^*(n')+O$ and that PFI-PEs observed at energies above the ion dissociation thresholds result

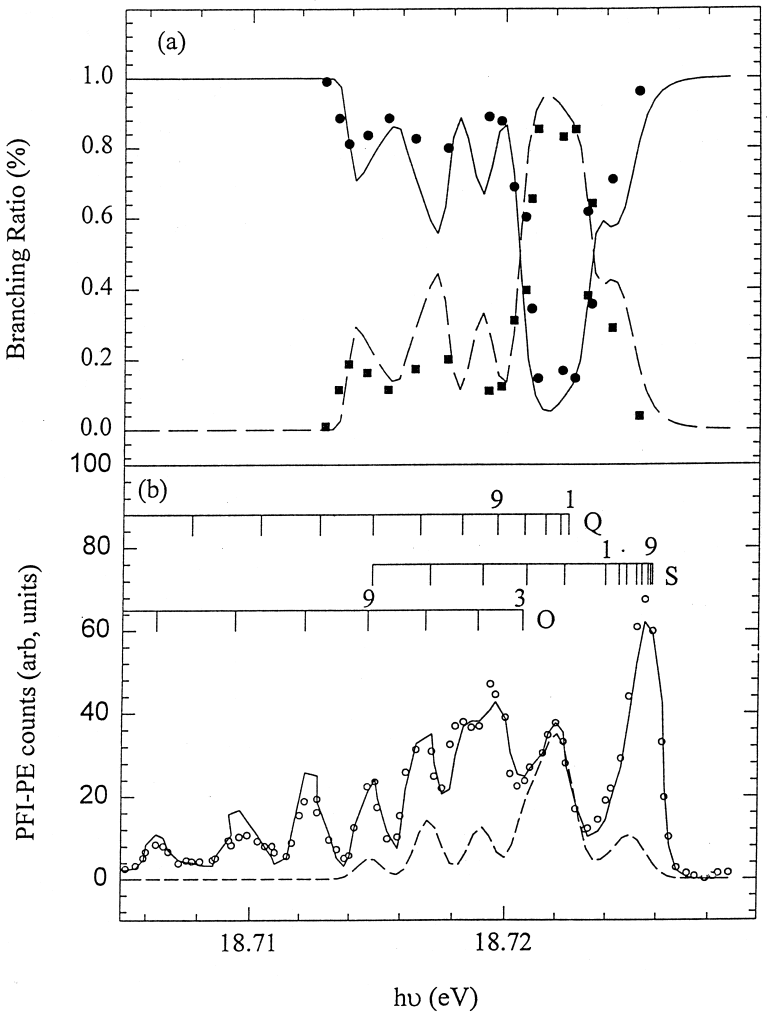

Fig. 8. (*a*) Breakdown diagram for the formation of $O^+(^4S)^+$ $O(^3P)$ from O_2 in the energy range of 18.705–18.730 eV [21]. The solid circles represent the branching ratios of O^+, and the solid squares are those for $O_2{}^+$. At a given photon energy, the sum of the branching ratios for O^+ and $O_2{}^+$ is normalized to 100. (*b*) PFI-PE spectrum (*open circles*) for $O_2{}^+(b^4\Sigma_g{}^-, v^+=4)$ in the energy range of 18.705–18.730 eV [15]. The simulation based on the BOS model is shown in solid line (see the text). The marking of the $\Delta N=-2$, 0, and +2 (or *O*, *Q*, and *S*, respectively) rotational branches are also shown in (*b*). The numbers given in (*b*) are N′′ values. The dashed line of (*b*) shows the population of $O_2{}^+(b^4\Sigma_g{}^-, v^+=4, N^+<9)$, estimated based on the simulation.

mostly from PFI of $O^*(n')$ [82,85,87]. Here, $O^*(n')$ represents an oxygen atom in a high-n' Rydberg state. In this case, the $O^*(n')$ state converges to the $O^+(^4S)$ limit, and the sequential steps for the PFI-PE formation are shown in process (10).

$$O_2 + h\nu \rightarrow O_2{}^*(n) \rightarrow O^*(n') + O(^3P)$$
$$\rightarrow O^+(^4S) + e^- + O(^3P) \qquad (10)$$

This dissociation-PFI mechanism is expected to be valid for high-*n* Rydberg states converging to a dissociative ion core with a dissociative lifetime shorter than the experimental time scale of $\approx 10^{-7}$ s. The dissociation lifetimes for $O_2{}^+(b^4\Sigma_g{}^-, v^+\geq 4)$ are known to be <4 ns [109−112].

If we assume that the population of $O_2{}^+(b^4\Sigma_g{}^-, v^+=4, N^+\geq 9)$ led to prompt dissociation, the popu-

lation for $O_2^+(b^4\Sigma_g^-, v^+=4, N^+<9)$ represents the intensity of O_2^+ observed in the PFI-PEPICO TOF spectrum. The calculated branching ratios for O^+ and O_2^+ are shown as the solid and dashed curves, respectively, in Fig. 8(a), which are found to be in good agreement with the experimental results. Two crossover points were observed in this breakdown diagram because the population of $Q(N^+>7)$ occurs on the low-energy side and that of $S(N^+>7)$ lies on the high-energy side of the $O_2^+(b^4\Sigma_g^-, v^+=4)$ band. The crossover point at 18.7207 eV locates between $Q(N^+=7$ and 9). The other crossover point at 18.7234 eV results from the population of N^+ (>7) levels via the S branch.

The experimental breakdown data shown in Fig. 8(a) indicate that complete dissociation of O_2^+ occurs at energies >18.7253 eV and <18.7129 eV and are consistent with the previous finding that the dissociation threshold for $O^+(^4S)+O(^3P)$ lies at $O_2^+(b^4\Sigma_g^-, v^+=4, N^+=9)$. The significance of this experiment is that it demonstrates the feasibility of selecting specific rotational states of diatomic ions for unimolecular and bimolecular reaction dynamics studies using this synchrotron-based PFI-PEPICO scheme.

2.5.3.2. The H-loss threshold for the dissociation of CH_4^+

For dissociation studies of polyatomic cations, the resolution of the PFI-PEPICO method is insufficient for the selection of specific rotational levels. As shown in the PFI-PEPICO study of CH_4, we have established that highly accurate AE values for some ion dissociation reactions can be determined by the disappearance energy of the parent ion [99].

Fig. 9 depicts selected PFI-PEPICO TOF spectra measured near the dissociation threshold for CH_3^+ from CH_4 [99]. At 13.9225 eV, only parent CH_4^+ ions are observed, whereas only daughter CH_3^+ ions are found at 14.3240 eV. As shown by the PFI-PEPICO TOF spectrum for $Ar^+(^2P_{3/2})$ in Fig. 6, the present ion TOF setup is sensitive to the ion E_{cm}. At 13.9225 eV, the CH_4^+ TOF peak is composed of a narrow and a broad component caused by photoionization of cold (≈30 K) CH_4 in the supersonic beam and thermal (298 K) background CH_4 in the photoionization

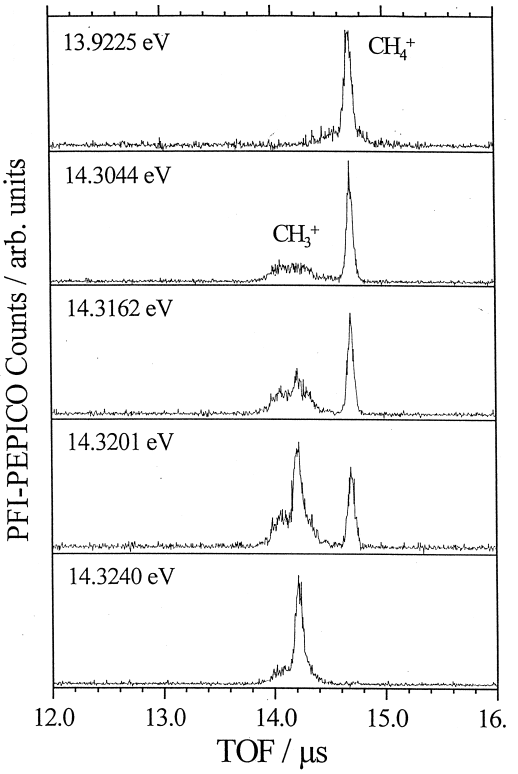

Fig. 9. PFI-PEPICO TOF spectra of CH_4 at $h\nu$=13.9225, 14.3044, 14.3162, 14.3201, and 14.3240 eV obtained using a dc electric background field of 1.3 V/cm [99]. The TOF peaks centered at 14.10 and 14.35 μs are caused by CH_3^+ and CH_4^+, respectively.

chamber, respectively. The ratio of these intensities for the cold and thermal CH_4 is found to be ≈85 : 15, which is similar to the cold/thermal ratio observed for the Ar system. As the $h\nu$ is increased to 14.3044 eV, a broad TOF peak for CH_3^+ was observed, concomitant with the disappearance of the broad thermal component for the CH_4^+ TOF peak. The TOF peak structures resolved in Fig. 9 unambiguously show that CH_3^+ formed at 14.3044 eV are mostly produced by dissociation of rotationally excited CH_4^+ formed in the photoionization of thermal CH_4. The narrow components of the TOF peak for CH_3^+ resulting from the dissociation of cold CH_4^+ are observed with increasing intensity as the $h\nu$ is increased from 14.3162 to 14.3201 and to 14.3240 eV.

Since the PFI-PEPICO TOF spectra resolve the dissociation caused by cold CH_4 from that of thermal

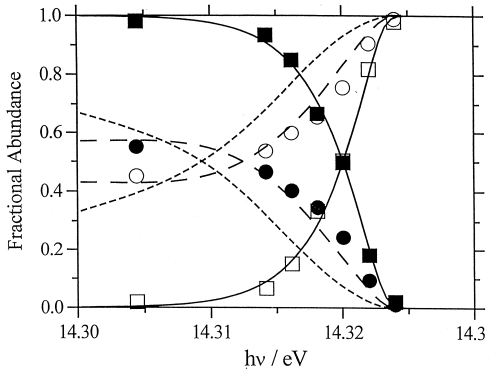

Fig. 10. Breakdown curves of CH_3^+ and CH_4^+ in the $h\nu$ range of 14.300−14.325 eV [99]. The experimental fractional abundances for CH_3^+ and CH_4^+ obtained based on the entire daughter ion signal are open circles and filled circles, whereas those obtained using only the cold daughter ion signal are indicated as open squares and filled squares, respectively. The lines are simulations curves: solid line, 33 K ensemble; closely dashed line, 33 K ensemble with 15% thermal background and 90% loss of parent ions; and loosely dashed line, 33 K ensemble with 15% thermal background and with an energy-dependent loss. See text.

CH_4, we have analyzed the TOF spectra by taking into account only the cold CH_3^+ ion signal based on the narrow TOF component. Fig. 10 shows the experimental breakdown data for CH_3^+ (open squares) and CH_4^+ (solid squares) in the $h\nu$ range of 14.300–14.323 eV [99]. As expected, these data form steep breakdown curves, which represent the dissociation of cold CH_4^+ formed by photoionization of supersonically cooled CH_4 (33 K). We were able to make excellent simulation of these breakdown curves. The 0 K AE(CH_3^+) thus determined is 14.323±0.001 eV [99].

The open and solid circular symbols in Fig. 10 show the respective fractional abundances of CH_3^+ and CH_4^+ derived by taking into account the cold and thermal components of CH_3^+. These breakdown data exhibit a considerable amount of fragmentation between 14.30 and 14.32 eV. Qualitatively, the main origin of this fragmentation signal arises from thermal CH_4^+ formed by photoionization of 298 K CH_4. However, the amount of fragmentation is significantly higher than the estimated thermal CH_4 background of ≈15% in the $h\nu$ range below the 0 K threshold. For example, at 14.316 eV the broad thermal CH_3^+ component accounts for nearly 50% of the total CH_3^+ signal. For the decay of CH_4*, there are two important competing decay channels, that is, autoionization and fragmentation. Clearly, in the PFI experiment only those CH_4* molecules that have survived autoionization and fragmentation for a time longer than the delay time for the application of the PFI pulse can be observed by PFI. Autoionization of CH_4* is accessible in the entire energy range studied since the energies are far above the IE of CH_4. If the CH_4^+ core is dissociative with a lifetime shorter than the delay time for the PFI pulse, prompt dissociation of CH_4* will occur to form CH_3*+H, where CH_3* represents CH_3 in a high-n Rydberg state. The pivotal point is that the CH_3* radicals formed by fragmentation of CH_4* near the dissociation threshold are preferentially formed below the IE of CH_3. Thus, we may conclude that autoionization is not readily accessible for CH_3* and is predominately operative for CH_4*. For CH_3* formed slightly above the dissociation threshold, it can also autoionize. However, the autoionization of this CH_3* may still be less probable than that of CH_4*.

On the basis of the above picture for the decay of CH_4*, we have performed simulation for the breakdown data by assuming that 90% of all CH_4* molecules formed below the dissociation threshold are lost because of autoionization [99]. Although this simulation (short-dashed lines in Fig. 10) represents a major improvement over all simulations neglecting this loss channel, the agreement with the experimental breakdown data including the entire ion signals (circles in Fig. 10) is by no means satisfying. Reasonable agreement between the experimental data and the simulation is obtained only if we assume that the amount of parent CH_4* lost because of autoionization varies with excitation energy. The long-dashed lines in Fig. 10 have been obtained assuming that the amount of all parent CH_4* lost decreases from ≈92% at 14.303 eV to ≈68% at 14.323 eV [99]. Since the rotational energy distribution of CH_4* is basically identical to that for CH_4 before photoexcitation, this assumption implies that the loss depends on the rotational angular momentum of CH_4. This variation of loss is most

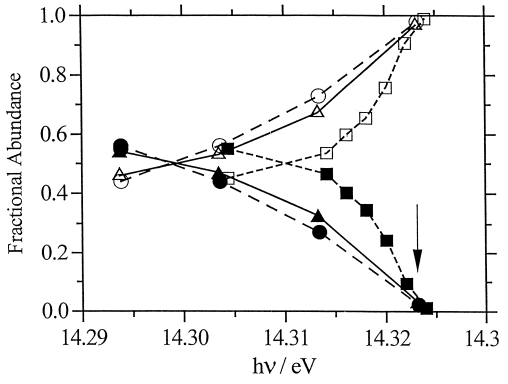

Fig. 11. Experimental breakdown data for CH_3^+/CH_4^+ based on total ion signals, which are measured at dc fields of 0.87 V/cm (*open triangles*/*solid triangles*), 1.30 V/cm (*open squares*/*solid squares*), and 1.74 V/cm (*open circles*/*solid circles*). Note that the disappearance energies for CH_4^+ are identical [99].

likely caused by a variation of the autoionization lifetime of CH_4*.

We have recorded experimental breakdown curves at different dc fields in the range of ≈0–2 V/cm (Fig. 11) [21,99]. The most striking observation is that the crossover energy is found to depend strongly on the dc Stark field. This observation indicates that the patterns of low-*n* interloper Rydberg states for CH_3 and CH_4 involved in the Stark ionization are different, resulting in different dc field dependencies for the PFI-PE intensities for CH_3^+ and CH_4^+. This effect is expected to be general for most molecules and may give rise to irregular structures of the experimental breakdown curves obtained in PFI-PEPICO TOF measurements [21,99].

Since the crossover energy depends on the Stark electric field in a PFI-PE study, this does not appear to be a good property for deriving 0 K AEs [21,99]. However, there is a unique feature, namely the disappearance energy of the parent molecule, in the PFI breakdown curve, which can be used to characterize the 0 K AE. As shown in Fig. 11, although the shapes and crossover points of the breakdown curves observed at different dc field are different, the disappearance energy for the parent CH_4^+ ion is found to be an intrinsic feature. The disappearance energy of the parent molecular ion is that energy, which even the coldest part of the neutral energy distribution reaches above the dissociation threshold. We emphasize that for the parent disappearance energy to serve as a true measure of the 0 K AE, the dissociation reaction must be prompt; that is, the dissociation lifetime of the excited parent species is shorter then the time scale ($\approx 10^{-7}$ s) of the present experiment. We note that in TPEPICO studies, where the threshold photoelectron measurements were affected by the hot-tail problem, the fractional abundance for the parent is not zero at the ion dissociation threshold. Thus, the disappearance energy for the parent ion observed in such TPEPICO studies cannot be used for the determination of 0 K AEs.

From the disappearance energy for CH_4^+ of Fig. 11, we derive a 0 K AE of 14.323±0.001 eV for the formation of CH_3^+ from CH_4. On the basis of previous PIE and TPEPICO studies, the 0 K AE(CH_3^+) varies in the range of 14.28–14.33 eV [58,113,114]. Although the present experiment is compatible with previous studies, it is characterized by a significantly higher accuracy. The adiabatic IEs of CH_3 (9.8357±0.00037 eV) [115] and CH_4 (12.618±0.004 eV) [116] have recently been accurately determined from rotationally resolved PFI-PE measurements. Combining these values with the present 0 K AE(CH_3^+) leads to D_0(H-CH_3)=4.487±0.001 eV and D_0(H-CH_3^+)=1.705±0.004 eV [99].

The necessary condition for obtaining accurate AE values in applying this PFI-PEPICO method is that the dissociation lifetime for the energy-selected parent ion is shorter than the time scale of the present experiment. This requirement limits the applicability of this method to small molecular ions with dissociation lifetimes of $\approx 10^{-7}$ s near the dissociation onset. We are in the process of installing a reflectron mass spectrometer for coincidence ion detection. Using such a spectrometer, ion dissociation lifetimes up to $\approx 10^{-3}$ s for energy-selected ion dissociation processes can be examined. Thus, we expect that the reflectron PFI-PEPICO apparatus can be applicable for accurate D_0 determination for larger molecular ions with a dissociation lifetime up to 10^{-3} to 10^{-4} s [53].

2.5.4. PFI-PI measurements

We have demonstrated that the synchrotron-based TOF selection method for PFI-PE detection [19] can also be applied for the detection of PFI-PIs using the two-bunch synchrotron radiation at the ALS [22], which has a dark gap of 328 ns. We have demonstrated the experimental scheme in the PFI-PI measurement of H_2 and Ar.

Referring to Eq. (9), the Δt value of an ion TOF peak is determined by the ion mass m, the average ion kinetic energy E_{cm} along the TOF axis, and the extraction electric field F at the PI/PEX region. We may view Δt as a measure of the dispersion of ions as they are transported from the PI/PEX region to the electron or ion detector. Because of the light mass of electrons, the small dispersion of prompt electrons and PFI-PEs results in the clear separation of the PFI-PE TOF peaks from prompt electrons, as shown in Fig. 2(c). The dispersion or Δt for H_2^+ is predicted to be ≈60-fold greater for the same E_{cm} and F values. As a consequence of the larger dispersion or Δt predicted for ions, background prompt ions formed by direct VUV photoionization and/or spontaneous autoionization are expected to extend into the dark gap, making the separation of PFI-PIs from prompt ions more difficult. The separation of PFI-PIs from background prompt ions using the TOF selection scheme would require a significantly larger dark gap than that used in PFI-PE measurements. For this reason, the PFI-PI measurements were performed at the two-bunch mode, where the dark gap is 328 ns.

The PFI and PFI-PI extraction conditions used are similar to those of the PFI-PEPICO study [21]. In the PFI-PI study [22], ion TOF spectra were recorded using a multichannel scaler (MCS) triggered by the bunch marker, a pulse sent out by the ALS for every VUV light bunch (328 ns). The procedures for the measurement of PFI-PI TOF spectra are basically the same as those for PFI-PEPICO TOF measurements, except that in the later measurement the MCS is triggered by the detection of an electron instead of a bunch marker.

The aspect concerning the influence of the PFI-PE and PFI-PI signals by the dc field maintained at the PI/PEX region has been discussed in detail previously [21]. Although the use of a larger F value reduces Δt, we found that it is necessary to set $F \leq 1.74$ V/cm to avoid a devastating loss of the PFI signal because of Stark ionization [21]. Thus, for a given ion mass, a practical mean for reducing the Δt value is to minimize E_{cm} by introducing the sample gas in the form of a supersonic beam.

2.5.4.1. PFI-PI band for $H_2^+(v^+=0, N^+ \leftarrow J'')$

Fig. 12(a) shows the TOF spectrum of H_2^+ (solid circles) taken at 15.4186 eV corresponding to the ($v^+=0$, $N^+=1 \leftarrow J''=1$) transition. Here, N^+ and J'' are the rotational quantum numbers for H_2^+ and H_2, respectively. The TOF spectrum of H_2^+ (solid squares) observed at the autoionization resonance at 15.4370 eV is plotted in Fig. 12(b). These spectra cover the region of one ALS period of 656 ns. Since there are no PFI-PIs formed at 15.4370 eV, the TOF spectrum reveals only two peaks caused by prompt ions centered at 215 and 543 ns, which can be attributed to H_2^+ formed by spontaneous autoionization and/or direct photoionization of H_2 in the supersonic beam. At 15.4186 eV, in addition to these two prompt ion peaks, two TOF peaks due to PFI-PIs of $H_2^+(N^+=1 \leftarrow J''=1)$ are found at 77 and 405 ns. As expected, both the prompt ion TOF peaks and the PFI-PI TOF peaks have a periodicity of 328 ns, which is identical to that of the VUV light bunch.

The TOF peaks for prompt H_2^+ ions observed at 15.4370 eV [Fig. 12(b)] have a FWHM of 46 ns. The simulation of these TOF peaks shows that the translational temperature attained for H_2 in the supersonic beam is ≈20 K. The dark gap, that is, the region between the adjacent TOF peaks for prompt H_2^+ ions, is nearly free of prompt H_2^+ ions. The finite prompt H_2^+ ions found at the dark gap are caused by H_2^+ produced by spontaneous autoionization and/or direct photoionization of thermal (298 K) background H_2 in the photoionization chamber. We have simulated the TOF spectra of Fig. 12(a) and 12(b) using two Gaussians functions with FWHMs of 46 and 200 ns to account for the cold (molecular beam, 20 K) and hot (thermal background, 298 K) H_2 samples. The simulated spectra (solid line) shown in Fig. 12(b) are

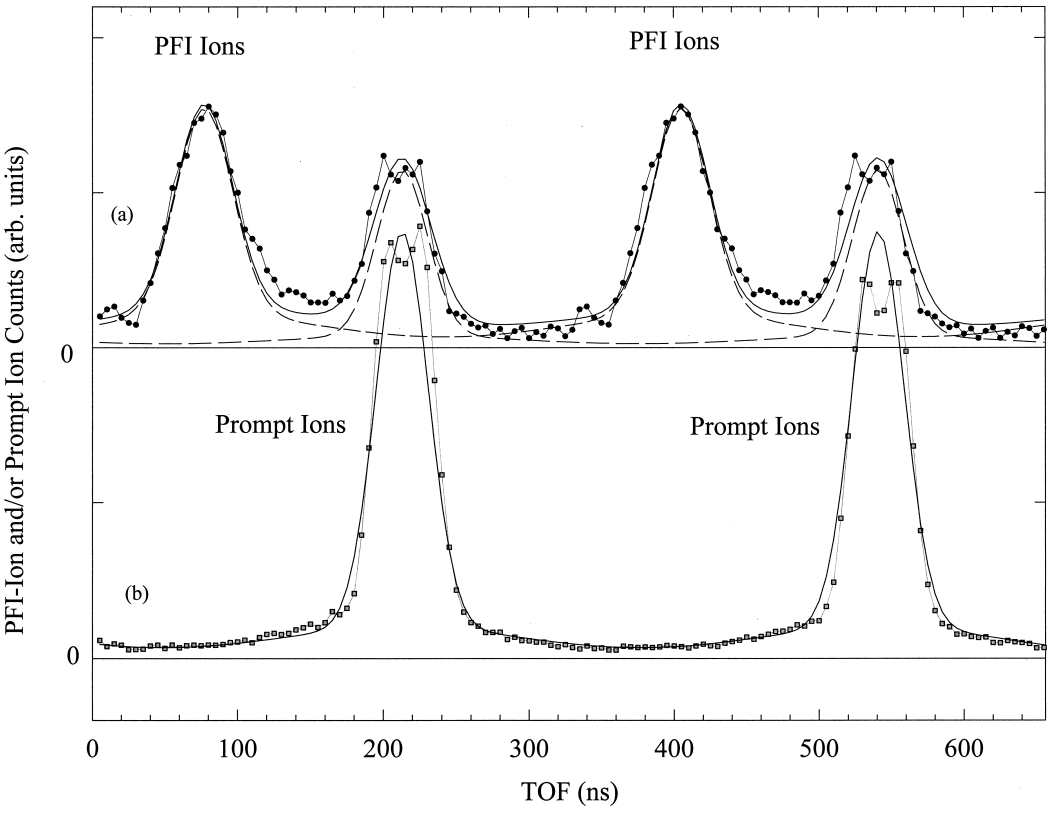

Fig. 12. TOF spectra for H_2^+ recorded at (*a*) 15.4186 eV (*solid circles*) and (*b*) 15.4370 eV (*solid squares*) [22]. These TOF spectra were recorded using the MCS triggered by the ALS bunch marker. Two Gaussian functions with FWHMs of 46 and 200 ns are used in the simulation to account for the cold (20 K) and hot (298 K) signals, respectively, observed in these spectra. The simulated spectra [*dashed curves* of (*a*)] for the prompt ions and PFI-PIs are obtained by assuming cold/hot ratios of 74 : 26 and 50 : 50, respectively. The overall simulation [*solid line* of (*a*)] represents the sum of the simulated contributions by the cold and hot signals. The simulated spectrum (*solid line*) of (*b*) is obtained by a cold/hot ratio of 74 : 26.

consistent with a ratio of 74 : 26 for the cold and hot signals.

As expected, by measuring the intensities for the prompt ion and PFI-PI peaks as a function of photon energy using an 80-ns time gate, we have obtained the spectra similar to the PIE spectrum for H_2^+ and PFI-PI spectrum for $H_2^+(v^+=0)$, respectively. After the correction of the background caused by prompt H_2^+ ions under the H_2^+ PFI-PI peak, we obtain the PFI-PI spectrum for H_2 shown in Fig. 13(b). The PFI-PE spectrum for H_2 obtained using a dc field of 4.3 V/cm and PFI field of 1.3 V/cm is depicted in Fig. 13(a) for comparison with this PFI-PI spectrum. Although the use of a higher-dc field of 4.3 V/cm was expected to lower the PFI-PI intensity, the choice of this dc field was necessary to yield a narrower TOF peak width for H_2^+. The positions of ionization rotational transitions (N^+, J'') are marked at the top of Fig. 13. Similar to the observation of the PFI-PE spectrum, the PFI-PI spectrum of Fig. 13(b) reveals rotational transitions of (0, 0), (1, 1), (2, 2), and (3, 3). The previous study shows that the relative intensities for rotational transitions in the PFI-PE spectrum of H_2 depend strongly on the dc electric field maintained at the PI/PEX region [117]. The weaker rotational transition (3, 3) observed in the PFI-PE spectrum of Fig. 13(a) compared to that of the PFI-PI spectrum of Fig. 13(b) can be attributed to the different dc fields used

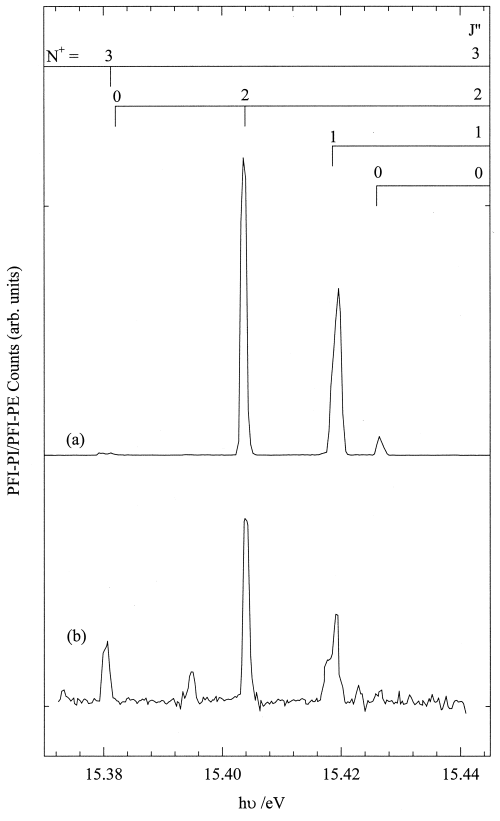

Fig. 13. Comparison of the (*a*) PFI-PE band and (*b*) PFI-PI band for $H_2^+(v^+=0, N^+\leftarrow J'')$ [22]. The positions of rotational transitions (N^+, J'') are marked at the top of the figure. The PFI-PE band is measured using a dc field of 4.3 V/cm and PFI field of 1.3 V/cm, whereas the PFI-PI band is obtained using a dc field of 1.74 V/cm and PFI field of 8.7 V/cm, together with background corrections as described in the text. The peaks at 15.395 and 15.423 eV observed in the PFI-PI band are attributed to residues of autoionization resonances.

in the PFI measurements. Although most of the residues caused by autoionization states are not observed in the PFI-PI spectrum, finite residues caused by autoionizing resonances at 15.395 and 15.423 eV are still discernible.

2.5.4.2. PFI-PI bands for $Ar^+(^2P_{3/2})$ and $Ar^+(^2P_{1/2})$

Fig. 14(a) shows the TOF spectrum of Ar^+ (solid circles) recorded at the IE (15.7560 eV) for the formation of $Ar^+(^2P_{3/2})$. The TOF spectrum (open squares) observed at the Ar(11s′) autoionization resonance, which lies at an energy 3.6 meV higher than the IE[$Ar^+(^2)P_{3/2}$], is depicted in Fig. 14(b). The latter TOF spectrum reveals two peaks centered at 281 and 609 ns, which are caused by prompt Ar^+ ions formed by direct photoionization and/or spontaneous autoionization. As predicted by Eq. (9), the width for these Ar^+ TOF peaks is significantly greater than those observed for the H_2^+ TOF peaks because of the higher mass for Ar^+. The large TOF dispersion of Ar^+ results in partial filling of the dark gap by prompt Ar^+ ions. Here, it is difficult to separate the components because of the cold and hot signals. We have simulated (solid line) the TOF spectrum of Fig. 14(b) using a Gaussian function with a FWHM of 180 ns.

The TOF spectrum for the PFI-PI Ar^+ ions shown in Fig. 14(a) has a similar pattern as that of prompt Ar^+ ions. The two PFI-PI peaks are found at 103 and 431 ns, corresponding to the centers of the dark gaps. We note that the positions at 281 and 609 ns in this spectrum, which correspond to the maxima of the prompt ion peaks in Fig. 14(b), are found to be minima. The TOF spectrum of Fig. 14(a) can be simulated by assuming a composition of 80% PFI-PIs and 20% prompt Ar^+ ions and by using the Gaussian function with a FWHM of 180 ns for the Ar^+ TOF distribution. The contributions of PFI-PIs and prompt ions are shown in Fig. 14(a) by dashed curves. The overall simulated spectrum (solid curve) represents the sum of these contributions.

Although the complete separation of the TOF peaks for Ar^+ PFI-PIs and prompt ions is not possible with the dark gap of 328 ns, the above simulation indicates that the contribution of background prompt ion signal at the PFI-PI peak can be reliably estimated. By employing a time gate of 100 ns centered at the Ar^+ PFI-PI ion peak, together with the correction of prompt ion background, we obtain the PFI-PI bands for $Ar^+(^2P_{3/2})$ and $Ar^+(^2P_{1/2})$ as shown in Fig. 15. The FWHMs of these bands show that the PFI-PI resolution achieved is about 1 meV (FWHM). The observed intensity ratio for the $Ar^+(^2P_{3/2})$ and $Ar^+(^2P_{1/2})$ PFI-PI bands is about 2 : 1, demonstrating that the detection of PFI-PIs resulting from the PFI of short-lived high-*n* Rydberg states, which converge to the excited $Ar^+(^2P_{1/2})$ threshold, is highly effiecient [17,19,82]. Thus, we may conclude that the PFI-PI

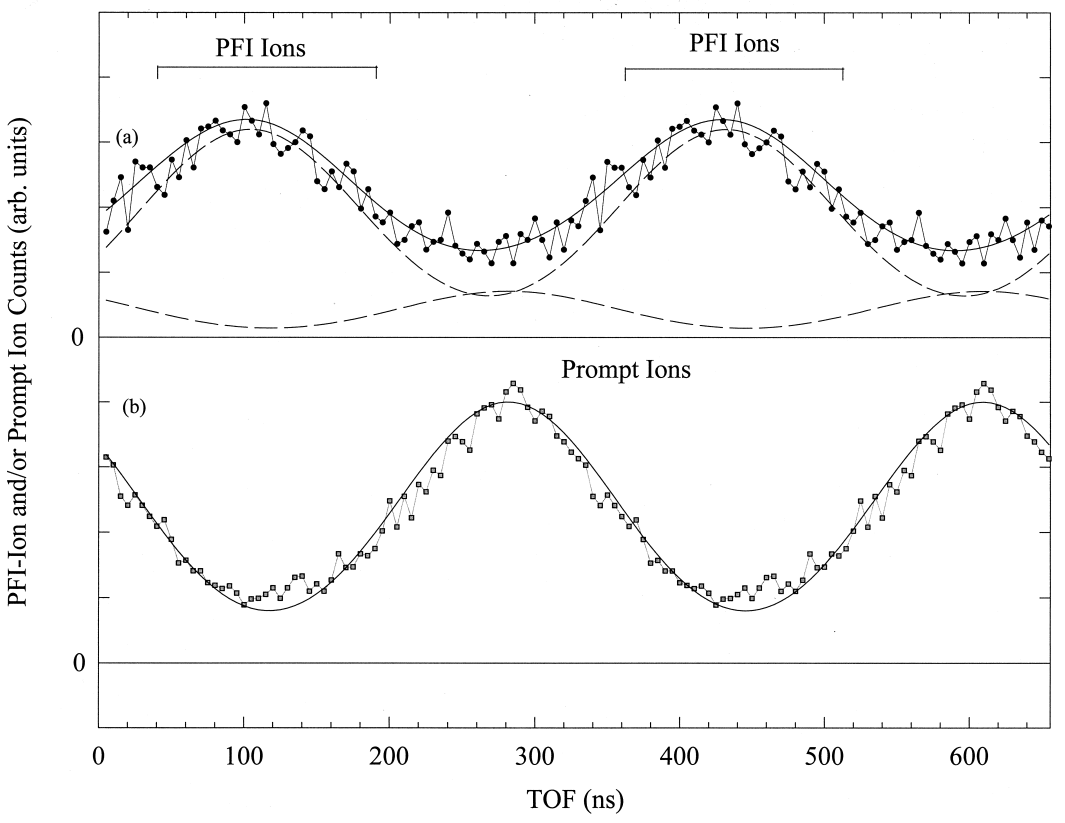

Fig. 14. TOF spectra for Ar^+ recorded at (*a*) the IE[$Ar^+(^2P_{3/2})$]=15.7596 eV (*solid circles*) and (*b*) at the Ar(11s′) autoionizing resonance at 15.7632eV (*open squares*), using a supersonic sample of ≈30 K [22]. The TOF spectra were recorded using the MCS triggered by the ALS bunch marker. The simulated spectra (*solid curves*) are obtained by using a Gaussian function with a FWHMs of 180 ns. The simulation shows that the TOF spectrum of (*a*) consists of 80% PFI-PIs and 20% prompt ions.

detection scheme described here is far superior to that used in our previous MATI study [17], where the PFI-PI band for $Ar^+(^2P_{1/2})$ was not observed.

For the PFI-PI measurement of Ar^+ and other ions with a higher mass than H_2^+, success would require the use of a larger dark gap. This can be achieved by mechanical chopping of the synchrotron VUV beam. If we use the same ion extraction and PFI conditions as described in this experiment, the clean separation of the PFI-PI and prompt Ar^+ ion peaks would require an on/off VUV pattern of ≈1.0 μs/1.0 μs. Since the dark gap required for PFI-PI measurements depends on the mass of the ion of interest, the use of a chopper wheel to chop the synchrotron beam is a sound approach because the dark gap can be adjusted to suit the experimental requirement [22].

3. Summaries and future prospects

In this article, we have summarized the recent progress in photoelectron-photoionization studies using VUV lasers and third-generation synchrotron radiation, such as the high-resolution monochromatized VUV undulator synchrotron source at the Chemical Dynamics Beamline of the ALS. The many new experimental techniques, including PFI-PE, PFI-PI, PFI-PEPICO, and PFI-IP schemes, established in the past decade ensure a bright future for high-resolution photoionization and photoelectron studies in the new millennium.

A profitable direction for photoionization mass spectrometry is to extend its application for the detection of biomolecules. De Vries and coworkers [118] have recently demonstrated the advantages of

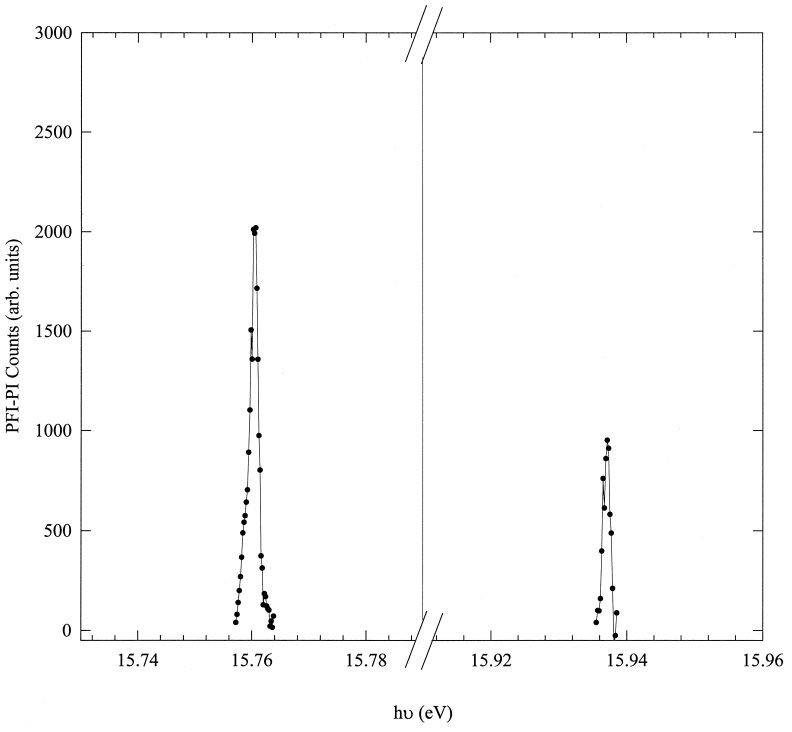

Fig. 15. PFI-PI bands for (*a*) $Ar^+(^2P_{3/2})$ and (*b*) $Ar^+(^2P_{1/2})$ obtained by measuring the PFI-PI intensity using a 100-ns time gate, together with background corrections described in the text [22]. Note that the ratio for the relative intensities for the $Ar^+(^2P_{3/2})$ and (*b*) $Ar^+(^2P_{1/2})$ PFI-PI bands is ∼2 : 1.

using VUV laser sources as ionization radiation for the sampling of biomolecules. However, the full potential in the application of tunable laser VUV radiation for the mass spectrometric sampling of biomolecules remains to be explored. The pulsed nature of VUV laser radiation makes it ideal for photoion analyses of biomolecules using the reflectron TOF technique.

The PD/PI experiments described in "PIE sampling of nascent photodissociation products" were demonstrated using a laboratory discharge lamp with VUV photon intensities in the range of $\approx 10^9$ to 10^{11} photons/s. The newly constructed high flux–medium resolution branchline of the Chemical Dynamics Beamline at the ALS is equipped with a 3-m monochromator, which is designed to have an intensity of $\approx 10^{14}$ photons/s with a resolving power of ≈1000. We expect that the PD/PI scheme can be used for probing the chemical structures of nascent photoproducts formed in photodissociation processes with a cross section down to $\approx 10^{-21}$ cm^2. It has been demonstrated that bond-selective dissociation can be realized via VUV excitation [119–121]. The selective bond breakage is attributed to excitation of a highly excited repulsive state of a specific bond. This results in prompt dissocation, avoiding the energy randomization process, which usually leads to the cleavage of the weakest chemical bond. The application of VUV photodissociation, together with VUV photoionization sampling, may provide structural information for biomolecules, particularly for biomolecules containing H–S, C–S, and S–S bonds [120–123].

The PIRI technique that combines the use of VUV synchrotron or VUV laser radiation to prepare intermediate long-lived high-*n* Rydberg species, along with tunable (IR, visible, UV, or VUV) laser radiation to induce ionization, holds great promise for further improvement in the energy resolution and energy

range in PFI studies. We also expect the PIRI method to become a useful technique for the preparation of state- or energy-selected ions for photodissociation and ion–molecule reaction studies. As pointed out above, synchrotron radiation is a pseudocontiuum light source. By using the synchrotron-based excitation method to prepare intermediate high–Rydberg states, we may use a very high resolution continuum wave (cw) dye laser as the photoionization source. In addition to the higher resolution offered by a cw laser compared to that for a pulsed laser, the use of a cw dye laser would also avoid the fragmentation of parent ions resulting from multiphoton processes [32].

Recently, we have employed the photofragment ion-imaging technique at the Chemical Dynamics Beamline of the ALS for the study of dissociative photoionization processes (11) and (12) in the photon energy range of 15–28 eV [124,125]:

$$SF_6 + h\nu \rightarrow SF_5^+ + F + e^- \quad (11)$$

$$\rightarrow SF_4^+ + 2F + e^- \quad (12)$$

This experiment represents the first application of the fragment ion-imaging technique in conjunction with synchrotron radiation. This technique allows direct inversion of the raw data to yield angular and translational energy distributions for the product ions. The analysis of the fragment ion angular distribution yields the anisotropy β parameter, providing detailed insight into the ion dissociation mechanisms. Although this is not a state- or energy-selected experiment, it provides addition information that cannot be easily obtained in a traditional TPEPICO study [126]. It is natural to combine the high-resolution VUV PEPICO method with the fragment ion-imaging scheme. A version of the ion-imaging PEPICO technique has recently been demonstrated [127]. However, the energy resolution achieved in this experiment is not high. Many variations of the imaging methods have been reported in the literature [124,125]. We may look forward to high-resolution ion-imaging PEPICO studies in the near future with parent ion internal state selection to the rotational level.

Acknowledgements

This work was supported by the Director, Office of Energy Research, Office of Basic Energy Sciences, Chemical Science Division of the U.S. Department of Energy under contract W-7405-Eng-82 for the Ames Laboratory and Contract DE-AC03-76SF00098 for the Lawrence Berkeley National Laboratory. Partial support by AFOSR is also acknowledged.

References

[1] H. Hurzeler, M.G. Inghram, J.D. Morrison, J. Chem. Phys. 28 (1958) 76.
[2] D. Villarejo, R. Herm, M. g. Inghram, J. Chem. Phys. 46 (1967) 4995.
[3] J. Berkowitz, Photoabsorption, Photoionization, and Photoelectron Spectroscopy, Academic Press, New York, 1979.
[4] H.M. Rosenstock, M.K. Draxl, B.W. Steiner, J.T. Herron, J. Phys. Ref. Data 6 (Suppl. 1) (1977).
[5] S.G. Lias, J.E. Bartmess, J.L. Holmes, R.D. Levin, and W.G. Mallard, J. Phys. Ref. Data 17 (Suppl. 1) (1988); ©The NIST Chemistry WebBook, http://webbook.nist.gov/chemistry/.
[6] C.Y. Ng (Ed.), Vacuum Ultraviolet Photoionization and Photodissociation of Molecules and Clusters, World Scientific, Singapore, 1991.
[7] I. Koyano, K. Tanaka, in: C.Y. Ng and M. Baer (eds.), State-Selected and State-to-State Ion–Molecule Reaction Dynamics I: Experiment, Advanced Chemical Physics, Vol. 82. Wiley, New York, 1992), p 263.
[8] I. Powis, T. Baer, C.Y. Ng (Eds.), High Resolution Laser Photoionization and Photoelectron Studies, Wiley Series in Ion Chemistry and Physics, Wiley, Chichester, 1995.
[9] E.W. Schlag, ZEKE Spectroscopy, Cambridge University Press, Cambridge, 1998.
[10] C. Y. Ng (Ed.), Photoionization and Photodetachment, Advanced Series in Physical Chemistry, Vols. 10A, 10B, World Scientific, Simgapore, 2000.
[11] J.W. Hepburn, in: C.Y. Ng (Ed.), Vacuum Ultraviolet Photoionization and Photodissociation of Molecules and Clusters, World Scientific, Singapore, 1991, p. 435.
[12] A.H. Kung, Y.T. Lee, in: C.Y. Ng (Ed.), Vacuum Ultraviolet Photoionization and Photodissociation of Molecules and Clusters, World Scientific, Singapore, 1991, p. 487.
[13] J.W. Hepburn, in: A. Meyers, T.R. Rizzo (Eds.), Laser Techniques in Chemistry, Wiley, New York, 1994.
[14] R.T. Wiedmann, M.G. White, in: I. Powis, T. Baer, C.Y. Ng (Eds.), High Resolution Laser Photoionization and Photoelectron Studies, Wiley Series in Ion Chemistry and Physics, Wiley, Chichester, 1995, p. 79, and references therein.
[15] P.A. Heimann, M. Koike, C.-W. Hsu, M. Evans, C.Y. Ng, D. Blank, X.-M. Yang, C. Flaim, A.G. Suits, Y.T. Lee, SPIE Proc. 2856 (1996) 90.

[16] C.Y. Ng, in: C.Y. Ng (Ed.), Photoionization and Photodetachment, Advanced Series in Physical Chemistry, Vol. 10A, World Scientific, Singapore, 2000 (Chapter 9), pp. 394–538.
[17] C.-W. Hsu, M. Evans, P. Heimann, K.T. Lu, C.Y. Ng, J. Chem. Phys. 105 (1996) 3950.
[18] P. Heimann, M. Koike, C.-W. Hsu, D. Blank, X.M. Yang, A. Suits, Y.T. Lee, M. Evans, C.Y. Ng, C. Flaim, H.A. Padmore, Rev. Sci. Instrum. 68 (1997) 1945.
[19] G.K. Jarvis, Y. Song, C.Y. Ng, Rev. Sci. Instrum. 70 (1999) 2615.
[20] C.-W. Hsu, P. Heimann, M. Evans, C.Y. Ng, Rev. Sci. Instrum. 68 (1997) 1694.
[21] G.K. Jarvis, K.-M. Weitzel, M. Malow, T. Baer, Y. Song, C.Y. Ng, Rev. Sci. Instrum. 70 (1999) 3892.
[22] G.K. Jarvis, R.C. Shiell, J. Hepburn, Y. Song, C.Y. Ng, Rev. Sci. Instrum. 71 (2000) 1325.
[23] R.I. Hall, A. McConkey, K. Ellis, G. Dawber, L. Avaldi, M.A. MacDonald, G.C. King, Meas. Sci. Technol. 3 (1992) 316.
[24] H. Palm, F. Merkt, Phys. Rev. Lett. 81 (1998) 1385.
[25] K. Müller-Dethlefs, M. Sander, E.W. Schlag, Chem. Phys. Lett. 112 (1984) 291.
[26] G. Reiser, W. Habenicht, K. Müller-Dethlefs, E.W. Schlag, Chem. Phys. Lett. 119 (1988) 152.
[27] L. Zhu, P. Johnson, J. Chem. Phys. 94 (1991) 5769.
[28] D. Taylor, J. Goode, J. LeClaire, P. Johnson, J. Chem. Phys. 103 (1995) 6293.
[29] D. Taylor, J. LeClaire, P. Johnson, Int. Mass Spectrom. Ion Proc. 159 (1996) 49.
[30] J. Goode, J. Hofstein, P. Johnson, J. Chem. Phys. 107 (1997) 1703.
[31] J. LeClaire, R. Anand, P. Johnson, J. Chem. Phys. 106 (1997) 6785.
[32] P. M. Johnson, in: C.Y. Ng (Ed.), Photoionization and Photodetachment, Advanced Series in Physical Chemistry, Vol. 10A, World Scientific, Singapore, 2000 (Chapter 7), p. 296.
[33] J.D.D. Martin, J.W. Hepburn, Phys. Rev. Lett. 79 (1997) 3154.
[34] J.D.D. Martin, J.W. Hepburn, J. Chem. Phys. 109 (1998) 8139.
[35] J.D. Hofstein, P.M. Johnson, Chem. Phys. Lett. 316 (2000) 229.
[36] C.Y. Ng, Adv. Chem. Phys. 52 (1983) 265–362.
[37] C.Y. Ng, Adv. Photochem. 22 (1997) 1.
[38] C.Y. Ng, in: T. Baer, C.Y. Ng, and I. Powis (Eds.), Structure, Energetics, and Reactivities of Organic Ions, Wiley Series in Ion Chemistry and Physics, Wiley, Chichester, 1996, p. 35.
[39] E.E. Mayer, E.R. Grant, J. Chem. Phys. 103 (1995) 10513.
[40] R.G. Neuhauser, K. Siglow, H.J. Neusser, J. Chem. Phys. 106 (1997) 896.
[41] R. Stebbings, F. Dunning, Rydberg States of Atoms and Molecules, Cambridge University Press, Cambridge, 1983.
[42] T. Gallagher, Rydberg Atoms, Cambridge University Press, Cambridge, 1994.
[43] S. Nourbakhsh, K. Norwood, G.-Z. He, C.Y. Ng, J. Am. Chem. Soc. 113 (1991) 6311.
[44] K. Norwood, S Nourbakhsh, G.-Z. He, C.Y. Ng, Chem. Phys. Lett. 184 (1991) 147.
[45] Z.-X. Ma, C.-L. Liao, H.-M. Yin, C.Y. Ng, S.-W. Chiu, I. Ma, W.-K. Li, Chem. Phys. Lett. 213 (1993) 250.
[46] Z.-X. Ma, C.-L. Liao, C.Y. Ng, Y.-S. Cheung, W.-K. Li, T. Baer, J. Chem. Phys. 100 (1994) 4780.
[47] C.-W. Hsu, C.-L. Liao, Z.-X. Ma, C.Y. Ng, J. Phys. Chem. 99 (1995) 1760.
[48] W.B. Peatman, T.B. Borne, E.W. Schlag, Chem. Phys. Lett. 3 (1969) 492; ©T. Baer, W.B. Peatman, E.W. Schlag, Chem. Phys. Lett. 4 (1969) 243.
[49] R. Sphor, P.-M. Guyon, W.A. Chupka, and J. Berkowitz, Rev. Sci. Instrum. 42 (1971) 1872.
[50] K. Kimura, S. Katsumata, Y. Achibi, T. Yamazaki, S. Iwata, Handbook of HeI Photoelectron Spectra of Fundamental Organic Molecules, Halsted Press, 1981.
[51] D.W. Turner, C. Baker, A.D. Baker, C.R. Brundle, Molecular Photoelectron Spectroscopy, Wiley, London, 1970.
[52] K.M. Weitzel, J. Mahnert, M. Penno, Chem. Phys. Lett. 224 (1994) 371.
[53] F. Güthe, K.-M. Weitzel, Ber. Bunsen-Ges. Phys. Chem. 104 (1997) 484.
[54] Y. Morioka, T. Tanaka, H. Yoshii, T. Hayaishi, J. Chem. Phys. 109 (1998) 1324.
[55] Y. Morioka, Y. Lu, T. Matsui, T. Tanaka, H. Yoshii, T. Hayaishi, R.I. Hall, J. Chem. Phys. 104 (1996) 9357.
[56] Y. Lu, Y. Morioka, T. Matsui, T. Tanaka, H. Hoshii, R.I. Hall, T. Hayaishi, K. Ito, J. Chem. Phys. 102 (1995) 1553.
[57] K.-M. Weitzel, J. Booze, T. Baer, Int. J. Mass Spectrom. Ion Proc. 107 (1991) 301.
[58] K.-M. Weitzel, Trends Chem. Phys. Res. Trends, 6 (1997) 143.
[59] T. Baer, in: M.T. Bowers (Ed.), Gas Phase Ion Chemistry, Vol. 1, Academic Press, New York, 1979, p. 153.
[60] T. Baer, Adv. Chem. Phys. 64 (1986) 111.
[61] T. Baer, J. Booze, K.-M. Weitzel, in: C.Y. Ng (Ed.), Vacuum Ultraviolet Photoionization and Photodissociation of Molecules and Clusters, World Scientific, Singapore, 1991, p. 259.
[62] K. Norwood, J.H. Guo, G. Luo, C.Y. Ng, J. Chem. Phys. 90 (1989) 6026.
[63] K. Norwood, A. Ali, C.Y. Ng, J. Chem. Phys. 95 (1991) 8029.
[64] K. Norwood, C.Y. Ng, Chem. Phys. Lett. 156 (1989) 145.
[65] C.Y. Ng, in: C.Y. Ng (Ed.), Vacuum Ultraviolet Photoionization and Photodissociation of Molecules and Clusters, World Scientific, Singapore, 1991, pp. 169–257.
[66] W. Kamke, in: C.Y. Ng, T. Baer, I. Powis (Eds.), Cluster Ions, Wiley, Chichester, 1993, p. 1.
[67] P.M. Guyon, T.R. Govers, T. Baer, Z. Phys. D 4 (1986) 89.
[68] P.M. Guyon, T. Baer, S.K. Cole, T.R. Govers, Chem. Phys. 119 (1988) 145.
[69] C.Y. Ng, in: J.M. Farrar. W. H. Saunders Jr. (Eds.), Techniques for the Study of Ion–Molecule Reactions, Wiley, New York, 1988, p. 417.
[70] A. Held, E.W. Schlag, Accts. Chem. Res. 31 (1998) 467.
[71] E.W. Schlag, R.D. Levine, Comments Atom. Mol. Phys. 33 (1997) 159.

[72] W.A. Chupka, J. Chem. Phys. 98 (1993) 4520; ©J. Chem. Phys. 99 (1993) 5800.
[73] S.T. Pratt, J. Chem. Phys. 98 (1993) 9241.
[74] A. Muhlpfordt, U. Even, J. Chem. Phys. 103 (1995) 4427.
[75] F. Merkt, J. Chem. Phys. 100 (1994) 2623; F. Merkt, R.N. Zare, J. Chem. Phys. 101 (1994) 3495.
[76] M.J.J. Vrakking, Y.T. Lee, J. Chem. Phys. 102 (1995) 883; © J. Chem. Phys. 102 (1995) 8818.
[77] S.R. Mackenzie, T.P. Softley, J. Chem. Phys. 101 (1994) 10609; ©F. Merkt, S.R. Mackenzie, T.P. Softley, J. Chem. Phys. 99 (1993) 4213.
[78] H.-T. Kim, R.J. Green, S.L. Anderson, J. Chem. Phys. 112 (2000) 10831.
[79] S.T. Pratt, E.F. McCormack, J.L. Dehmer, P.M. Dehmer, Phys. Rev. Lett. 68 (1992) 584.
[80] A. Fujii, A. Iwasaki, T. Ebata, N. Mikami, J. Phys. Chem. 101 (1997) 5963.
[81] C.-W. Hsu, M. Evans, S. Stimson, C.Y. Ng, P. Heimann, J. Chem. Phys. 106 (1997) 8931.
[82] C.-W. Hsu, P. Heimann, M. Evans, S. Stimson, C.Y. Ng, Chem. Phys. 231 (1998) 121.
[83] S. Stimson, M. Evans, C.Y. Ng, C. Destandau, G. Chambaud, P. Rosmus, C.-W. Hsu, P. Heimann, J. Chem. Phys. 108 (1998) 6205.
[84] C.-W. Hsu, M. Evan, S. Stimson, C.Y. Ng, J. Chem. Phys. 108 (1998) 4701.
[85] C.-W. Hsu, M. Evans, S. Stimson, C.Y. Ng, J. Chem. Phys. 109 (1998) 1285.
[86] S. Stimson, Y.-J. Chen, M. Evans, C.-L. Liao, C.Y. Ng, C.-W. Hsu, P. Heimann, Chem. Phys. Lett. 289 (1998) 507.
[87] M. Evans, S. Stimson, C.Y. Ng, C.-W. Hsu, G.K. Jarvis, J. Chem. Phys. 110 (1999) 315.
[88] G.K. Jarvis, Y. Song, C.Y. Ng, J. Chem. Phys. 111 (1999) 1937.
[89] Y. Song, M. Evans, C.Y. Ng, C.-W. Hsu, G.K. Jarvis, J. Chem. Phys. 111 (1999) 1905.
[90] G.K. Jarvis, M. Evans, C.Y. Ng, K. Mitsuke, J. Chem. Phys. 111 (1999) 3058.
[91] D. Fedorov, M. Evans, Y. Song, M. Gordon, C.Y. Ng, J. Chem. Phys. 111 (1999) 6413.
[92] M. Evans, C.Y. Ng, J. Chem. Phys. 111 (1999) 8879.
[93] G.K. Jarvis, Y. Song, C.Y. Ng, E.R. Grant, J. Chem. Phys. 111 (1999) 9568.
[94] R.C. Shiell, M. Evans, S. Stimson, C.Y. Ng, J.W. Hepburn, Chem. Phys. Lett. 315 (1999) 390.
[95] Y. Song, M. Evans, C.Y. Ng, C.-W. Hsu, G.K. Jarvis, J. Chem. Phys. 112 (2000) 1271.
[96] Y. Song, M. Evans, C.Y. Ng, C.-W. Hsu, G.K. Jarvis, J. Chem. Phys. 112 (2000) 1306.
[97] A. Yencha, M.C.A. Lopes, G.C. King, M. Hochlaf, Y. Song, C.Y. Ng, Faraday Discussion 115, April 3–5, 2000.
[98] J. Liu, W. Chen, C.-W. Hsu, M. Hochlaf, M. Evans, S. Stimson, C.Y. Ng, J. Chem. Phys. 112 (2000) 10767.
[99] K.-M. Weitzel, M. Malow, G.K. Jarvis, T. Baer, Y. Song, C.Y. Ng, J. Chem. Phys. 111 (1999) 8267.
[100] G.K. Jarvis, K.-M. Weitzel, M. Malow, T. Baer, Y. Song, C.Y. Ng, Phys. Chem. Chem. Phys. 1 (1999) 5259.
[101] T. Baer, Y. Song, C.Y. Ng, W. Chen, J. Liu, *J. Phys. Chem. 104 (2000) 1959.*
[102] T. Baer, Y. Song, C.Y. Ng, J. Liu, W. Chen, Faraday Discussion 115 (2000) 137.
[103] K. Raghavachar, B.B. Stefanov, L.A. Curtiss, J. Chem. Phys. 106 (1997) 6764.
[104] D.P. Chong, C.Y. Ng, J. Chem. Phys. 98 (1993) 759.
[105] A.G. Suits, P. Heimann, X.-M. Yang, M. Evans, C.-W. Hsu, K.-T. Lu, Y.T. Lee, A.H. Kung, Rev. Sci. Instrum. 66 (1995) 4841.
[106] H. Palm, F. Merkt, Phys. Rev. Lett. 81 (1998) 1385.
[107] H.-J. Diederich, K. Müller-Dethlefs, L.Y. Baranov, Phys. Rev. Lett. 76 (1996) 3530.
[108] P. Dehmer, W.A. Chupka, J. Chem. Phys. 65 (1976) 2243.
[109] P.C. Cosby, J.-B. Ozenne, J.T. Moseley, D.L. Albritton, J. Mol. Spect. 79 (1980) 203.
[110] J.T. Moseley, P.C. Cosby, J.-B. Ozenne, J. Durup, J. Chem. Phys. 70 (1979) 1474.
[111] J.C. Hansen, J.T. Moseley, A.L. Roche, P.C. Cosby, J. Chem. Phys. 77 (1982) 1206.
[112] H. Helm, P.C. Cosby, D.L. Huestis, J. Chem. Phys. 73 (1980) 2629.
[113] W.A. Chupka, J. Chem. Phys. 48 (1968) 2337.
[114] K.E. McCulloh, V.H. Dibeler, J. Chem. Phys. 64 (1976) 4445.
[115] J.A. Blush, P. Chen, M.G. White, J. Chem. Phys. 98 (1993) 3557.
[116] R. Signorell, F. Merkt, J. Chem. Phys. 110 (1999) 2309.
[117] G. Jarvis, Y. Song, C.Y. Ng, to be published.
[118] E. Nir, H.E. Hunziker, M.S. de Vries, Anal. Chem. 71 (1999) 1674.
[119] J.S. Keller, P.W. Kash, E. Jensen, L.J. Butler, J. Chem. Phys. 96 (1992) 4324.
[120] L.J. Butler, E.J. Hintsa, S.F. Shane, Y.T. Lee, J. Chem. Phys. 86 (1987) 2951.
[121] S. Nourbakhsh, K. Norwood, H.-M. Yin, C.-L. Liao, C.Y. Ng, J. Chem. Phys. 95 (1991) 946.
[122] S. Nourbakhsh, C.-L. Liao, C.Y. Ng, J. Chem. Phys. 92 (1990) 6587.
[123] S. Nourbakhsh, K. Norwood, H.-M. Yin, C.-L. Liao, C.Y. Ng, J. Chem. Phys. 95 (1991) 5014.
[124] D.S. Peterka, M. Ahmed, C.Y. Ng, A.G. Suits, Chem. Phys. Lett. 312 (1999) 108.
[125] M. Evans, C.Y. Ng, C.-W. Hsu, P. Heimann, J. Chem. Phys. 106 (1997) 978.
[126] D.H. Parker, in: C.Y. Ng (Ed.), Photoionization and Photodetachment, Advanced Series in Physical Chemistry, Vol. 10A, World Scientific, Singapore, 2000 (Chapter 1), p. 3.
[127] A. Lafosse, M. Lebech, J.C. Brenot, P.M. Guyon, O. Jagutzski, L. Spielberger, M. Vervloet, J.C. Houver, D. Dowek, Phys. Rev. Lett. 84 (2000) 5987.